KTH Information and
Communication Technology

Design and Characterization of Plasmonic Absorbers Based on Gold Nano-spheres

JIN DAI

Master's Thesis
Supervisor: Dr. Min Yan
Examiner: Prof. Min Qiu

TRITA-ICT-EX-2012: 106

Abstract

Noble-metal-based nanostructures can exhibit strong localized plasmon resonance at optical frequency, which leads to efficient plasmonic light absorbers. Such an artificially engineered absorber can have potential applications in sensing, cancer diagnosis and therapy, and photovoltaic cells etc. This thesis systematically studies a particular class of plasmonic absorber based on gold nanoparticles deposited on top of a continuous gold substrate. In our case studies, the nanoparticles have sub-wavelength sizes of less than 50 nm; their reflectances are examined over 400-800 nm light wavelength range. With a 3D finite-element method, we identified that the resonance at especially a long-wavelength position originates not from dipole resonance of the particles, but from the inter-particle near-field coupling resonance. The influences of particle size, particle shape, inter-particle distance, particle-substrate spacer, particle lattice, number of particle layers etc on the resonance are studied thoroughly. Experimentally, an absorber based on chemically-synthesized Au@SiO2 core-shell nanoparticles was fabricated. Measurement shows that the absorber has a characteristic absorption band around 800 nm with an absorbance peak of $\sim$90%, which agrees surprisingly well with our numerical calculation. The fabrication technique can be easily scaled for devising efficient light absorbers of large areas.

Acknowledgements

First, I would like to give special thanks to Erasmus Mundus MSc in Photonics consortium for supplying me the perfect opportunity to start my academic exploration in Photonics and also the 2 years' enjoyable life.

During my first year's study at Ghent University, I have learnt a lot from all the professors who gave us lectures. I benefit a lot from Prof. Kristiaan Neyts's impressive Optical Materials course. Also I need to thank Prof. Roel Baets and Prof. Heidi Ottevaere for giving me a lot valuable suggestions.

For my thesis work, no one else deserves more thanks than Dr. Min Yan, who is the supervisor of my thesis. First, I need to thank him for sharing his experience in COMSOL with me. He also teaches me a lot of knowledge in Plasmonics and numerical simulation. Second, I need to thank him for providing me the opportunities to work in the cleanroom at KTH. He is also a good friend who makes the research become more interesting. Also I would like to thank Prof. Min Qiu for giving me the chance to work on this interspersing topic. Besides, I need to thank Fei Ye who prepares the Au@Si_2 core-shell particles for me. Without his well prepared nanoparticles, I cannot get this well performed absorber. Also I need to Yiting Chen for his kind help in the lab.

I would like to thank all my classmates, and everyone in Nanophotonics group at KTH. I have had a memorable time during my study and my thesis work.

At last, I need to give special thanks to my family and all my friends. Their kind help and encouragement support me to overcome any difficulties I meet in my life.

June 2012

Jin Dai

Usage permissions

June 2012

Jin Dai

Contents

Chapter 1

Introduction

1.1 Plasmonic absorbers

Optical metamaterials (MMs) are artificially structured materials with nanoscale inclusions and strikingly unconventional properties at optical frequencies [1]. Noble metals, like copper, silver, and gold are used as excellent mirror materials since ancient time. However, when they are patterned in subwavelength nanostructure, the reflectance may disappear because light can be transferred to the collective electron excitations and henceforth damped through collision with lattice. The collective electron oscillation excited by optical frequency electromagnetic wave is known as localized surface plasmon resonances (LSPR) [2]. This resonant frequency strongly depends on the size, shape, dielectric properties, and the surrounding dielectric environment of the nanoparticles [3]. Thanks to the modern nanofabrication technique such as electron-beam lithography (EBL) [4], focused-ion beam milling [5], or self-assembly of colloids [6], the applications of optical properties of LSPR have been explored enormously in recent years. For example, based on the dependence of dielectric environment, Liu et al. demonstrated a perfect absorber as plasmonic sensor for refractive index sensing [7]. Also, a

lot of research has focused on utilizing the energy absorption process to enhance the efficiency of photovoltaic cells [8]. However, for a traditional metal-insulator-metal(MIM) structure absorber operating in the visible regime, the dimensions of the nanoparticles are under 50 nm. Even with EBL process, it's a formidable task to fabricate these tiny particles, especially when it comes to fabricate large sample.

Recently, a perfect plasmonic absorber in a stack of metal and nanocomposite showing almost 100% absorbance covering all the visible spectra range has been demonstrated by Hedayati et al. [9]. It is fabricated by a cost-effective method and compatible with current industrial methods for microelectromechanical systems (MEMS). Absorbers fabricated in this way can be cheap and flexible. The goals of this thesis are, first to simulate of this kind of nano-spheres based absorber to investigate all the factors that may affect the optical response, and second to design, fabricate ,and characterize a novel absorber based on Au@SiO_2 core-shell nanoparticles.

1.2 Overview of the thesis

In this thesis, Chapter 2 will introduce the electromagnetic theory of metal and the background knowledge of LSPR. Effect of mean free path (MFP) on dielectric properties of nano-spheres with diameter under 10 nm will also be introduced.

Chapter 3 focuses on the simulation results of the reported perfect plasmonic absorber [9]. We will start with briefly introducing the numerical method used in our simulations. It is followed by effects of several factors on the optical response of the absorber.

In chapter 4, we propose a novel designed absorber based on nano-spheres. We will also show the optical characterization of the fabricated absorber.

Chapter 2

Plasmonics

2.1 Introduction

The high absorbance of the plasmonic absorber is due to LSPR, which is basically caused by interaction of electromagnetic field with metallic nanoparticles. This interaction can be well understood in the classical electromagnetic theory based on Maxwell's equations. We will start with a briefly review of Maxwell equations and several models of dielectric function of metal. The chapter will end with the theory behind LSPR and effect of MFP.

2.2 Maxwell's equations

According to classical electromagnetism, light is electromagnetic radiation, which can be describe using two fields: the electric field $\boldsymbol{E}(\boldsymbol{r}, t)$ and the magnetic induc-

tion field $\boldsymbol{B}(\boldsymbol{r}, t)$. Both of them are governed by Maxwell's equations:

$$\nabla \cdot \boldsymbol{E} = \frac{1}{\epsilon_0}\rho_a \tag{2.1a}$$

$$\nabla \cdot \boldsymbol{B} = 0 \tag{2.1b}$$

$$\nabla \times \boldsymbol{E} = -\frac{\partial \boldsymbol{B}}{\partial t} \tag{2.1c}$$

$$\nabla \times \boldsymbol{B} = \mu_0 \boldsymbol{J_a} + \epsilon_0 \mu_0 \frac{\partial \boldsymbol{E}}{\partial t} \tag{2.1d}$$

in which ρ_a is the charge density due to both separate charges and polarization charges, and $\boldsymbol{J_a}$ is the current density due to free currents, currents related to polarization charge and current related to magnetization.

By introducing two new fields: the electric displacement field $\boldsymbol{D}$ and the magnetic field $\boldsymbol{H}$:

$$\boldsymbol{D} = \epsilon_0 \boldsymbol{E} + \boldsymbol{P} \tag{2.2a}$$

$$\boldsymbol{H} = \frac{\boldsymbol{B}}{\mu_0} - \boldsymbol{M} \tag{2.2b}$$

Maxwell's equations in matter can then be written as:

$$\nabla \cdot \boldsymbol{D} = \rho \tag{2.3a}$$

$$\nabla \cdot \boldsymbol{B} = 0 \tag{2.3b}$$

$$\nabla \times \boldsymbol{E} = -\frac{\partial \boldsymbol{B}}{\partial t} \tag{2.3c}$$

$$\nabla \times \boldsymbol{H} = \boldsymbol{J} + \frac{\partial \boldsymbol{D}}{\partial t} \tag{2.3d}$$

Here, the source terms ρ and $\boldsymbol{J}$ contain only the free charges and free currents respectively. In order to a solvable system, we have to find a relationship between $\boldsymbol{P}$ and $\boldsymbol{E}$ and between $\boldsymbol{M}$ and $\boldsymbol{B}$, which is given by constitutive relation.

Since we consider only nonmagnetic material, the magnetization field vanishes:

$$\boldsymbol{M} = 0 \tag{2.4}$$

then we get:

$$\boldsymbol{B} = \mu_0 \boldsymbol{H} \tag{2.5}$$

Most materials contain electrical dipoles or are polarized due to electric field. Consequently, $\boldsymbol{P}$ should be a function of electric field $\boldsymbol{E}$. Expand it into Taylor series we get [10]:

$$\boldsymbol{P} = \boldsymbol{P}^{(0)} + \boldsymbol{P}^{(1)} + \boldsymbol{P}^{(2)} + \dots \tag{2.6}$$

in which $\boldsymbol{P}^{(0)}$ is the static polarization, independent of electric field. $\boldsymbol{P}^{(1)}$ is the first-order polarization, which is proportional to the electric field. $\boldsymbol{P}^{(2)}$ is the second-order polarization, proportional to square of the electric field and so on.

In general the nth order polarization is

$$\begin{aligned} P_i^{(n)}(\boldsymbol{r}, t) = \quad & \epsilon_0 \iiint_V \mathrm{d}\boldsymbol{r}_1 \cdots \iiint_V \mathrm{d}\boldsymbol{r}_n \int_{-\infty}^{\infty} dt_1 \cdots \int_{-\infty}^{\infty} \mathrm{d}t_n \chi^n_{ij_1\cdots j_n}(\boldsymbol{r}, \boldsymbol{r}_1, \dots \\ & \boldsymbol{r}_n, t, t_1, \dots, t_n) E_{j_1}(\boldsymbol{r}_1, t_1) \cdots E_{j_n}(\boldsymbol{r}_n, t_n) \end{aligned} \tag{2.7}$$

with $\chi^{(n)}$ the nth order susceptibility which is a tensor of rank n+1. If we assume that the materials are homogeneous and stationary, the constitutive relation can

be rewritten as:

$$P_i^{(n)}(\boldsymbol{r},t) = \epsilon_0 \iiint_V \mathrm{d}\boldsymbol{r}_1 \cdots \iiint_V \mathrm{d}\boldsymbol{r}_n \int_{-\infty}^{\infty} \mathrm{d}t_1 \cdots \int_{-\infty}^{\infty} \mathrm{d}t_n \chi^n_{ij_1\cdots j_n}(\boldsymbol{r}-\boldsymbol{r}_1,\ldots \\ \boldsymbol{r}-\boldsymbol{r}_n, t-t_1,\ldots,t-t_n) E_{j_1}(\boldsymbol{r}_1,t_1)\cdots E_{j_n}(\boldsymbol{r}_n,t_n) \quad (2.8)$$

To make it simple, we further assume that the material is linear and isotropic, which means only the first-order of all the susceptibilities remain and the polarization field must always be parallel to electric field, then we get:

$$\boldsymbol{P}(\boldsymbol{r},t) = \epsilon_0 \iiint_V \mathrm{d}\boldsymbol{r}_1 \int_{-\infty}^{\infty} \mathrm{d}t_1 \chi^{(1)}(\boldsymbol{r}-\boldsymbol{r}_1, t-t_1) E(\boldsymbol{r}_1,t_1) \quad (2.9)$$

Applying Fourier transform, the constitutive relation in the frequency domain becomes:

$$\boldsymbol{P}(\boldsymbol{k},\omega) = \epsilon_0 \chi(\boldsymbol{k},\omega)\boldsymbol{E}(\boldsymbol{k},\omega) \quad (2.10)$$

substitution of (2.10) in (2.2a) gives:

$$\boldsymbol{D} = \epsilon_0(1+\chi(\boldsymbol{k},\omega))\boldsymbol{E}(\boldsymbol{k},\omega) = \epsilon_0\epsilon_r(\boldsymbol{k},\omega)\boldsymbol{E}(\boldsymbol{k},\omega) \quad (2.11)$$

in which ϵ_r is the relative permittivity of the material. Inserting it into (2.3) for a material without free charge, currents or magnetization yields

$$\nabla \cdot \boldsymbol{D} = 0 \quad (2.12a)$$

$$\nabla \cdot \boldsymbol{B} = 0 \quad (2.12b)$$

$$\nabla \times \boldsymbol{E} = -\frac{\partial \boldsymbol{B}}{\partial t} \quad (2.12c)$$

$$\nabla \times \boldsymbol{B} = -\epsilon_0\epsilon_r\mu_0 \frac{\partial \boldsymbol{E}}{\partial t} \quad (2.12d)$$

Taking the curl of (2.12c) and substituting the time derivative of (2.12d) yields

$$\nabla \times (\nabla \times \boldsymbol{E}) = -\epsilon_o \epsilon_r \mu_0 \frac{\partial^2 \boldsymbol{E}}{\partial t^2} \tag{2.13}$$

From vector calculus we know that

$$\nabla \times \nabla \times \boldsymbol{E} = \nabla(\nabla \cdot \boldsymbol{E}) - \nabla^2 \boldsymbol{E} \tag{2.14}$$

Further manipulation leads to:

$$\nabla(\nabla \cdot \boldsymbol{E}) - \nabla^2 \boldsymbol{E} + \epsilon_r(\boldsymbol{k}, \omega)\frac{\omega^2}{c^2}\boldsymbol{E} = 0 \tag{2.15}$$

For transverse wave, $\nabla(\nabla \cdot \boldsymbol{E}) = 0$, Eq. (2.15) yields

$$\nabla^2 \boldsymbol{E} - \epsilon_r(\boldsymbol{k}, \omega)\frac{\omega^2}{c^2}\boldsymbol{E} = 0 \tag{2.16}$$

Introducing

$$k^2 = \epsilon_r \frac{\omega^2}{c^2} \tag{2.17}$$

one has

$$\nabla^2 \boldsymbol{E} - k^2 \boldsymbol{E} = 0 \tag{2.18}$$

For longitudinal waves, Eq. (2.15) implies that

$$\epsilon_r(\boldsymbol{k}, \omega) = 0 \tag{2.19}$$

indicating that longitudinal wave solution occurs at frequencies corresponding to $\epsilon_r(\omega) = 0$.

2.3 Dielectric function of nobel metals

2.3.1 Drude free-electron model

In order to investigate the interaction between electric field and metallic nanoparticles, we have to know the optical response of metal, which is described by ϵ_r in the eigenvalue problem (2.16).

In 1900, Paul Drude developed a theory to explain the electrical and thermal conductivities in metal [11, 12]. Drude model takes a metal as a free gas of electrons and applies kinetic theory of gases. In our discussion of the Drude model, we shall simply assume that, in the formation of a metal, the valence electrons become detached and wander freely through the metal, while the metallic ions remain intact and act as immobile positive particles, as show in Fig. 2.1.

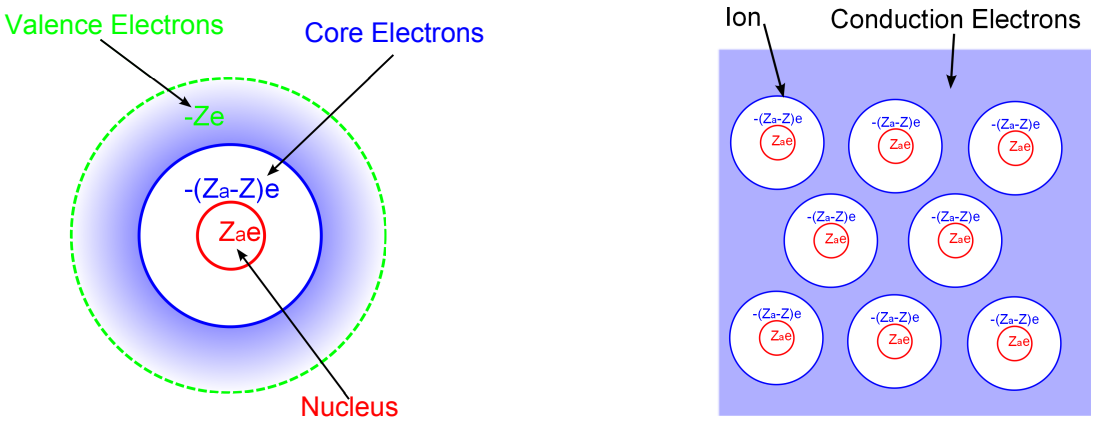

Figure 2.1. (a) Metal atom; (b) View of metal in Drude model.

Several basic assumptions have been made in Drude model [13, 14]: (1) Between collisions, the interaction of a given electron, both with the others and with the ions, is neglected. Fig. 2.2 shows schematically the trajectory of a scattering conduction electron. (2) Collisions in the Drude model, as that in kinetic the-

ory, are instantaneous events that abruptly alter the velocity of an electron. (3) An electron experiences a collision with a probability per unit time $1/\tau$ and the collision probability in time interval is $\mathrm{d}t/\tau$. τ is the collision time, relaxation time or the mean free time, which can be expressed by $1/\tau = v_F/l_\infty$. v_F is the Fermi velocity and l_∞ is the bulk mean free path of the material. (4) Electrons are assumed to achieve thermal equilibrium with their surroundings only through collisions. These collisions are assumed to maintain local thermodynamic equilibrium in a particularly simple way: immediately after each collision an electron is taken to emerge with a velocity that is not related to its velocity just before the collision, but randomly directed and with a speed appropriate to the temperature prevailing at the place where the collision occurred.

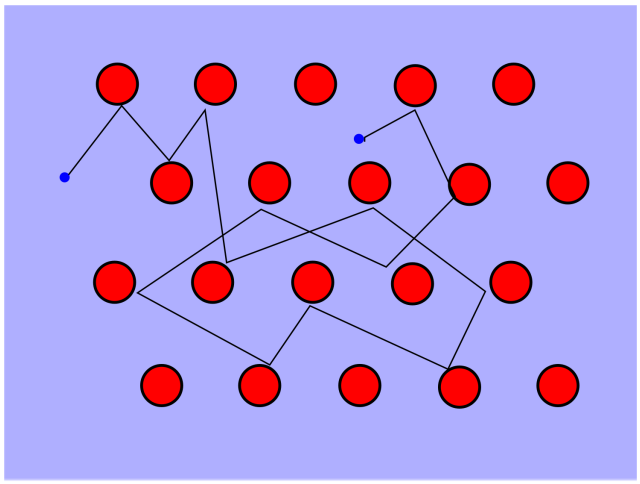

Figure 2.2. Trajectory of a conduction electron scattering off the ions

According to the assumptions, the momentum increase if no collision occurred between t and $t + \mathrm{d}t$ is

$$\boldsymbol{p}_{nocoll}(t + \mathrm{d}t) = (1 - \frac{\mathrm{d}t}{\tau})[\boldsymbol{p}(t) + \boldsymbol{f}(t)\mathrm{d}t + O((\mathrm{d}t)^2)] \tag{2.20}$$

in which $1 - \frac{\mathrm{d}t}{\tau}$ is the fraction of the total number of electrons that do not collide and $\boldsymbol{f}(t)$ is the force acting on the electron.

For the electrons that undergo collisions between t and $t + \mathrm{d}t$, the momentum increase is

$$\boldsymbol{p}_{coll}(t + \mathrm{d}t) = \frac{\mathrm{d}t}{\tau}[\boldsymbol{f}(t)\mathrm{d}t + O((\mathrm{d}t)^2)] \tag{2.21}$$

Combing (2.20) and (2.21) and rearranging it, we have

$$\frac{\boldsymbol{p}(t + \mathrm{d}t) - \boldsymbol{p}(t)}{\mathrm{d}t} = -\frac{1}{\tau}\boldsymbol{p}(t) + \boldsymbol{f}(t) \tag{2.22}$$

Taking the limit $\mathrm{d}(t) \to 0$, we obtain

$$\frac{\mathrm{d}\boldsymbol{p}(t)}{\mathrm{d}t} = -\frac{1}{\tau}\boldsymbol{p}(t) + \boldsymbol{f}(t) \tag{2.23}$$

Form (2.23), we see that the effect of individual electron collision introduce a damping term into the equation of motion for the momentum per electron. To see the response of metal to electric field, we assume that the metal is subject to a electric field, which has only a Fourier component

$$\boldsymbol{E}(t) = Re[\boldsymbol{E}(\omega)e^{-j\omega t}] \tag{2.24}$$

The force on electrons then can be written as

$$\boldsymbol{f}(t) = -e\boldsymbol{E}(t) \tag{2.25}$$

Substitution of (2.25) into (2.23) yields

$$\frac{\mathrm{d}\boldsymbol{p}}{\mathrm{d}t} = -\frac{1}{\tau}\boldsymbol{p} - e\boldsymbol{E} \tag{2.26}$$

Seeking a solution of the form $\boldsymbol{p}(t) = Re[\boldsymbol{p}(\omega)e^{-j\omega t}]$, we obtain

$$-j\omega\boldsymbol{p}(\omega) = -\frac{1}{\tau}\boldsymbol{p}(\omega) - e\boldsymbol{\omega} \tag{2.27}$$

thus,

$$\boldsymbol{p}(\omega) = -\frac{e\boldsymbol{E}(\omega)}{1/\tau - j\omega} \tag{2.28}$$

From $\boldsymbol{j}(t) = -ne\boldsymbol{p}(t)/m$, we have

$$\boldsymbol{J}(w) = -\frac{ne\boldsymbol{p}(\omega)}{m} = \frac{ne^2m}{1/\tau - jw}\boldsymbol{E}(\omega) \tag{2.29}$$

Comparing (2.29) with Ohm's law

$$\boldsymbol{J}(\omega) = \sigma(\omega)\boldsymbol{E}(\omega), \tag{2.30}$$

we obtain

$$\sigma(\omega) = \frac{ne^2\tau}{m}\frac{1}{1 - j\omega\tau} \tag{2.31}$$

Then the relative permittivity becomes:

$$\epsilon_r(\omega) = 1 + \frac{j\sigma(\omega)}{\epsilon_0\omega} = 1 - \frac{ne^2}{m\epsilon_0}\frac{1}{\omega^2 + j\omega/\tau} \tag{2.32}$$

Introducing plasmon frequency $\omega_p^2 = \frac{ne^2}{\epsilon_0 m}$ and collision frequency $\gamma = 1/\tau$, we obtain

$$\epsilon_r(\omega) = 1 - \frac{\omega_p^2}{\omega^2 + j\omega\gamma} \tag{2.33}$$

For nobel metals, like Au, the response to electric field is dominated by free electrons in s band in the region $\omega > \omega_p$, since the filled d band close to the Fermi surface causes a highly polarized environment. This effect can be described by a dielectric constant ϵ_∞, and we can write

$$\epsilon_r(\omega) = \epsilon_\infty - \frac{\omega_p^2}{\omega^2 + j\omega\gamma} \tag{2.34}$$

Usually, ϵ is in the range of 1 to 10. The dielectric function described by free electron model is shown in Fig. 2.3 (a) and (b).

2.3.2 Lorentz oscillator model

In Eq. (2.34), only free electron gas model and the polarization of the ion core have been taken into consideration. However, for nobel metals like gold, silver or copper, interband transition occurs at high frequency. For gold, the electronic configuration is $5d^{10}6s^1$. And threshold of transition from d band into conduction band is approximate 2.38 ev, which lies somewhere in the green part of visible spectrum. As a result, Eq. (2.38) cannot describe the optical properties properly in the visible regime. In Lorentz's theory, such interband transition can be describe as a restoring force modeled by Hooke's law.

$$F = -k\boldsymbol{r} = -m\boldsymbol{r}\omega_0^2 \tag{2.35}$$

Then, in the time-dependent electric field, the motion of an electron oscillator can be written as

$$\frac{\mathrm{d}^2\boldsymbol{r}}{\mathrm{d}t^2} + \gamma\frac{\mathrm{d}\boldsymbol{r}}{\mathrm{d}t} + \omega_0^2\boldsymbol{r} = -\frac{e\boldsymbol{E}_0}{m}e^{-jwt} \tag{2.36}$$

We now find the solution of the form $\boldsymbol{r} = \boldsymbol{r}_0 e^{-j\omega t}$. The solution is then given by

$$\boldsymbol{r} = \frac{(e\boldsymbol{E}_0/m)e^{-j\omega t}}{\omega^2 - \omega_0^2 + j\gamma\omega} \tag{2.37}$$

Each oscillator carries a dipole moment $\boldsymbol{p} = -e\boldsymbol{r}$, then the polarization density is given by

$$\boldsymbol{P} = n\boldsymbol{p} = -ne\boldsymbol{r} = \frac{(ne^2\boldsymbol{E}_0/m)e^{-j\omega t}}{\omega_0^2 - \omega^2 - j\gamma\omega} \tag{2.38}$$

From the definition of polarizability $\alpha = \boldsymbol{P}/\boldsymbol{E}$, we get

$$\alpha = \frac{ne^2/m}{\omega_0^2 - \omega^2 - j\gamma\omega} \tag{2.39}$$

Substitution of (2.39) into Clausius-Mossotti relation yeilds

$$\epsilon(\omega) \approx 1 - \frac{Ne^2/m}{\omega_0^2 - \omega^2 - j\gamma\omega} \tag{2.40}$$

In metal, each oscillator contributes differently in general. To characterize the contributions of different oscillators, we introduce the oscillator strength f_j for the$j$th order of oscillator with the natural frequency ω_j and the damping lefttime $1/\gamma$.Taking contributions from all oscillators into account, we have

$$\epsilon_{r-oscillator}(\omega) = \sum_{j=1}^{k} \frac{f_j\omega_p^2}{(\omega_j^2 - \omega^2) + j\omega\gamma_j} \tag{2.41}$$

Thus, the relative permittivity of gold can written as

$$\epsilon_r(\omega) = \epsilon_\infty - \frac{\omega_p^2}{\omega^2 + j\omega\gamma} + \sum_{j=1}^{k} \frac{f_j\omega_p^2}{(\omega_j^2 - \omega^2) - j\omega\gamma_j} \tag{2.42}$$

Table 2.1. Values of the LD Model Parameters for gold

f_1	γ_1^α	ω_1^α	f_2	γ_2^α	ω_2^α	f_3	γ_3^α	ω_3^α
0.025	0.241	0.415	0.010	0.345	0.830	0.071	0.870	2.969
f_4	γ_4^α	ω_5^α	f_5	γ_5^α	ω_5^α			
0.601	2.494	4.304	4.384	2.214	13.32			

[α]In electron volts

Using the date get from experimental measurements that was given in table 2.1 [15], we plot the real and imaginary part of relative permittivity of gold as shown in Fig. 2.3(a) and (b), respectively. After considering the interband transitions and core effects, the model fits the experimental results [16].

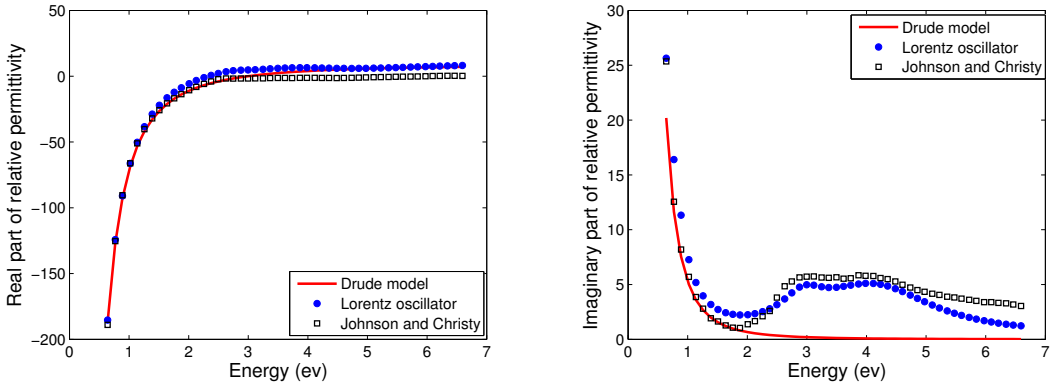

(a) (b)

Figure 2.3. (a) Real part of relative permittivity of gold; (b) Imaginary part of relative permittivity of gold.

2.3.3 Effect of mean free path

All the discussions above are based on bulk metal, we haven't taken any size effects into consideration. However, if the size of the particle is smaller than the mean free path of electrons in the metal, the electrons will scatter at the particle surface, which leads to a modification of the dielectric function of the metal. The

additional scattering process made the size-dependent effective mean free path l_R smaller than the bulk mean free path l_∞.

Several approaches has been reported to calculate l_R. The common character of them is that the additional contribution to bulk collision frequency γ_∞ is proportional to $1/R$. Thus, the modified size-dependent collision frequency can be expressed by

$$\gamma_{mod} = \gamma_\infty + \triangle\gamma(R) = \gamma_\infty + A\frac{v_F}{R} \tag{2.43}$$

in which R is the radius of the spherical nanoparticle, and A, which is affected by the shape and the surface condition of the nanoparticle, is used to account for the angular nature of the electron scattering. As shown in Fig. 2.3, the dielectric properties of realistic metal can be described by (2.42), which is approximately equal to the experimental results . We replace the collision frequency by (2.43), then we get the modified relative permittivity [17]

$$\epsilon(\omega, R) = \epsilon_{epx} + \frac{\omega_p^2}{\omega^2 + j\omega\gamma} - \frac{\omega_p^2}{\omega^2 + j\omega\gamma_{mod}} \tag{2.44}$$

Here the ϵ_{epx} we use is from Johnson and Chrisy's paper [16] and the plots of relative permittivity of gold sphere for $R = 3nm$, and $R = 4nm$ with $A = 1.2$ are shown in Fig. 2.4. The mean free path effect does not affect the real part of the relative permittivity so much, however comparing to the bulk material, the imaginary part increases due to the size effect. In addition, the increase is larger for smaller particle size.

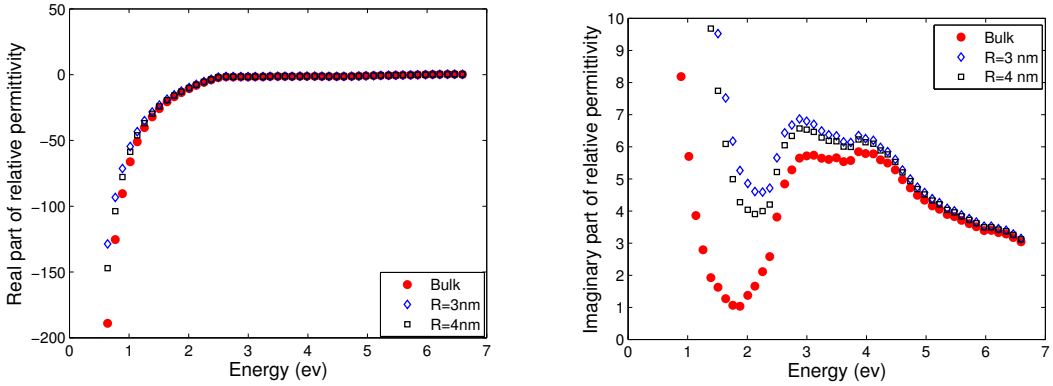

(a) (b)

Figure 2.4. (a) Real part of size-dependent relative permittivity of gold sphere; (b) Imaginary part of size-dependent relative permittivity of gold sphere.

2.4 Localized surface plasmon resonances

Localized surface plasmons are none propagating excitations of the conduction electrons of metallic nanostructures coupled to the electromagnetic field [18]. Consider a metallic structure whose size is much smaller the wavelength of the electromagnetic field. When such a metallic structure interacts with an oscillating electromagnetic field the field both inside and near-field zone outside the structure is enhanced due to the resonance of electrons on the its surface. The resonance is called the LSPR.

2.4.1 Mie theory

To investigate the interaction between a metallic structure with oscillating electromagnetic field we have to solve the Maxwell's equations. According to Mie [19] or Debye's [20] work on the diffraction problem of a single sphere, the scalar elec-

tromagnetic potentials ψ are the solutions of

$$\nabla^2\psi + k^2\psi = 0 \tag{2.45}$$

which has the form of Helmholtz Equation. Writing in spherical coordinate system gives

$$\frac{1}{r^2}\frac{\partial}{\partial r}(r^2\frac{\partial\psi}{\partial r}) + \frac{1}{r^2\sin\theta}\frac{\partial}{\partial\theta}(\sin\theta\frac{\partial\psi}{\partial\theta}) + \frac{1}{r^2\sin\theta}\frac{\partial^2\psi}{\partial\phi^2} + k^2\psi = 0 \tag{2.46}$$

Separating the variables to find solutions of the form

$$\psi(r,\theta,\phi) = R(r)\Theta(\theta)\Phi(\phi) \tag{2.47}$$

we obtain three separated equations:

$$\frac{\mathrm{d}^2\phi}{\mathrm{d}\phi^2} + m^2\phi = 0 \tag{2.48}$$

$$\frac{1}{\sin\theta}\frac{\mathrm{d}}{\mathrm{d}\theta}(\sin\theta\frac{\mathrm{d}\Theta}{\mathrm{d}\theta}) + [l(l+1) - \frac{m^2}{\sin^2\theta}]\Theta = 0 \tag{2.49}$$

$$\frac{\mathrm{d}}{\mathrm{d}r}(r^2\frac{\mathrm{d}R}{\mathrm{d}r}) + [k^2r^2 - l(l+1)]R = 0 \tag{2.50}$$

Mathematically, the general solutions can be written as

$$\psi(r,\theta,\phi) = \left\{ \begin{array}{c} \cos(m\phi) \\ \sin(m\phi) \end{array} \right\} \cdot \left\{ \begin{array}{c} \sqrt{\frac{\pi}{2x}}J_{l+\frac{1}{2}}(x) \\ \sqrt{\frac{\pi}{2x}}N_{l+\frac{1}{2}}(x) \end{array} \right\} \cdot P_l^m(\cos\theta) \tag{2.51}$$

in which $m = 0, 1, 2\cdots l$, $l = 0, 1, 2\cdots$, and $x = kr$. $P_l^m(\cos\theta)$ is the associated

Legendre polynomials. J and N are spherical Bessel functions. By applying appropriate boundary conditions and rewriting the incident electromagnetic wave in the form of multipole expansions, we can get the field distribution [19]. The solutions consist of two parts, the field inside the sphere, and the field outside the sphere which includes the incident filed and the scattered field. The total Mie extinction spectrum contains dipolar, quadrupolar and higher modes of electronic excitation. Each multipole contributes to the scattering and absorption loss [17].

2.4.2 Quasi-static approximation of sub-wavelength metal particle

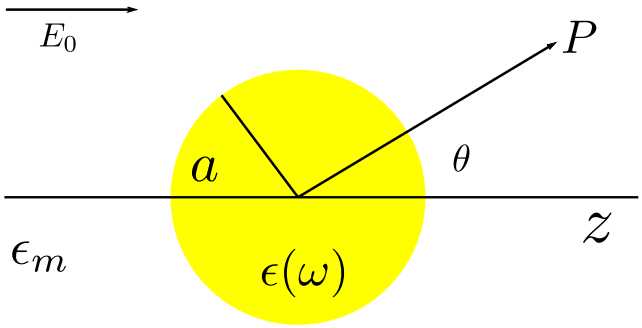

Figure 2.5. Nano-sphere in electrostatic field

Mie theory can give us the exact solution of the scattering problem of spheres, however the math is cumbersome. Considering a sphere with a radius a, which much more smaller than the wavelength, embedded in a nonconducting material, the phase retardation of the oscillating field over the sphere can be neglected. Thus the field can be approximately treated as an electrostatic field $\boldsymbol{E} = E_0\hat{\boldsymbol{z}}$ as shown in Fig. 2.5. ϵ_m and $\epsilon(\omega)$ are the relative permittivity of the surrounding medium and that of the sphere respectively. By introducing the potential ϕ, we can write the electric field as $-\nabla\phi$. To get the electric field distribution, we firstly

need to get ϕ, which is the solution of Laplace equation

$$\nabla^2\phi = 0 \tag{2.52}$$

Assuming the sphere is isotropic and homogeneous, thus it is symmetric in the azimuthal direction. The general solution is given by

$$\phi(r,\theta) = \sum_{l=0}^{\infty}[A_l r^l + B_l r^{-(l+1)}]P_l(\cos\theta) \tag{2.53}$$

In which P_l is Legendre polynomials of the lth order. We first start will the potential inside the sphere. When $r \to 0$, the potential should be finite. So we obtain $B_l = 0$. The solution inside the sphere becomes

$$\phi_{in}(r,\theta) = \sum_{l=0}^{\infty} A_l r^l P_l(\cos\theta) \tag{2.54}$$

For the field outside the sphere at a distance $r \gg a$, the term $B_l r^{-(l+1)} P_l(\cos\theta)$ in (2.53) is smaller enough to be omitted. We obtain

$$\phi_{out}(r,\theta) = \sum_{l=0}^{\infty} C_l r^l P_l(\cos\theta) \tag{2.55}$$

And from electrostatic field theory we have

$$\phi_{out}|_{r\to\infty} \sim -E_0 r\cos\theta = -E_0 r P_1(\cos\theta) \tag{2.56}$$

Comparing (2.55) to (2.56) we obtain

$$C_1 = E_0, C_l = 0. \quad (l \neq 0, 1) \tag{2.57}$$

The solution outside the sphere then can be written as

$$\phi_{out} = C_0 - E_0 r P_1(\cos\theta) + \sum_{l=0}^{\infty} D_l \frac{1}{r^{l+1}} P_l(\cos\theta) \tag{2.58}$$

The continuous of potential at the interface between the sphere and the surrounding medium yields

$$\phi_{in}|_{r=a} = \phi_{out}|_{r=a} \tag{2.59}$$

Moreover, the continuous of normal component of displacement gives

$$\epsilon_0 \epsilon_m \frac{\partial \phi_{out}}{\partial r}|_{r=a} = \epsilon_0 \epsilon \frac{\partial \phi_{in}}{\partial r}|_{r=a} \tag{2.60}$$

Substitution of (2.59) (2.60) into (2.54) (2.58) and comparing the coefficient of the same order yields

$$\begin{cases} D_0 = 0, \\ C_0 = A_0; \end{cases} \quad \begin{cases} A_1 = -\frac{3\epsilon_m}{\epsilon+2\epsilon_m}, \\ C_1 = \frac{\epsilon-\epsilon_m}{\epsilon+2\epsilon_m} a^3 E_0; \end{cases} \quad \begin{cases} A_l = 0, \\ B_l = 0; \end{cases} \quad (l \neq 0, 1) \tag{2.61}$$

then the solution becomes

$$\begin{cases} \phi_{in} = A_0 - \frac{3\epsilon_m}{\epsilon+2\epsilon_m} E_0 r \cos\theta, \\ \phi_{out} = A_0 - E_0 r \cos\theta + \frac{\epsilon-\epsilon_m}{\epsilon+2\epsilon_m} a^3 E_0 \frac{1}{r^2} \cos\theta. \end{cases} \tag{2.62}$$

By introducing dipole moment

$$\boldsymbol{p} = 4\pi\epsilon_0\epsilon_m \frac{\epsilon - \epsilon_m}{\epsilon + 2\epsilon_m} \boldsymbol{E}_0 \tag{2.63}$$

the potential outside the sphere can be rewritten as

$$\phi_{out} = A_0 - E_0 r\cos\theta + \frac{\boldsymbol{p}\cdot\boldsymbol{r}}{4\pi\epsilon_0\epsilon_m r^3} \tag{2.64}$$

Comparing (2.63) to

$$\boldsymbol{p} = \epsilon_0\epsilon_m\alpha\boldsymbol{E}_0 \tag{2.65}$$

yields

$$\alpha = 4\pi a^3\frac{\epsilon-\epsilon_m}{\epsilon+2\epsilon_m} \tag{2.66}$$

in which α describe the polarizability of the nano-sphere. The resonance occurs at

$$Re[\epsilon(\omega)] = -2\epsilon_m \tag{2.67}$$

which is also called Fröhlich condition [18] and the mode is the dipole surface plasmon. Applying $\boldsymbol{E} = -\nabla\phi$ on (2.62) gives us the electric field distribution

$$\begin{cases} \boldsymbol{E}_{in} = \frac{3\epsilon_m}{\epsilon+2\epsilon_m}\boldsymbol{E}_0 \\ \boldsymbol{E}_{out} = \boldsymbol{E}_0 + \frac{3\boldsymbol{n}(\boldsymbol{n}\cdot\boldsymbol{p})-\boldsymbol{p}}{4\pi\epsilon_0\epsilon_m}\frac{1}{r^3} \end{cases} \tag{2.68}$$

The fields both inside and outside the sphere are enhanced due to the dipole resonance. Bohren and Huffman [21] also give the expression for cross section of

scattering C_{sca} and absorption C_{abs}

$$C_{sca} = \frac{8\pi}{3} k^4 a^6 \left| \frac{\epsilon - \epsilon_m}{\epsilon + 2\epsilon_m} \right|^2 \tag{2.69a}$$

$$C_{abs} = 4\pi k a^3 Im\left[\frac{\epsilon - \epsilon_m}{\epsilon + 2\epsilon_m} \right] \tag{2.69b}$$

The extinctions efficiency Q_ext can be describe by

$$Q_{ext} = \frac{C_{ext}}{S} = \frac{C_{sca} + C_{abs}}{\pi a^2} \tag{2.70}$$

in which πa^2 represent the geometrical square of the spherical particle. Fig. 2.6(a) shows the extinction efficiency of spherical gold particle, with a radius of 5nm,embedded in silica (refractive index 1.5) for both with and without considering MFP effect. Fig. 2.5(b) shows the extinction for the particle in silica and air. From the figures we obtain that the MFP effect broaden the extinction spectrum and lower the peak and the increase of the dielectric function of the surrounding medium leads to the red-shifts of the LSPR.

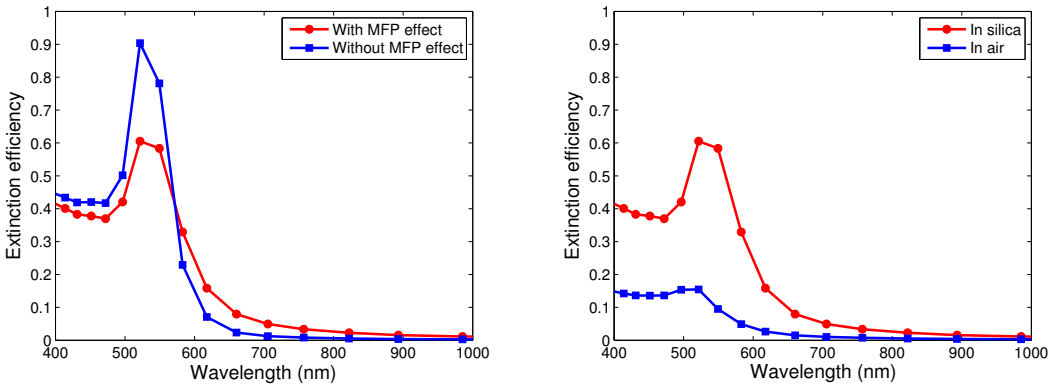

(a) (b)

Figure 2.6. Extinction efficiency of spherical gold particle embedded (a) in silica with and without considering MFP effect; (b) in air and silica.

Chapter 3

Simulation Results and Discussion

3.1 Introduction

In this chapter, we will mainly study the properties of nano-sphere absorbers based on the broadband abosrber which is demonstrateed by Hedayati et al. [9]. In the paper, they explained that the broadband absorption was attributed to two factors: one is the coupling between the broad Mie resonance of the nanoparticles, the other is the interaction within the nanoparticle plasmon resonances in the composite and their dipole images on the gold reflector. However, there are two more factors may also lead to the resonance of the absorber, the dipole resonance of individual nanoparticle, and the Fabry-Pérot resonance [22]. Additionally, in the range about from 400 nm to 500 nm, the interband transition of gold will also contribute to the high absorption.

In our work, we use numerical method to investigate which resonance contributes to the broad and high absorption of the absorber through looking into the field distribution at resonant frequencies. The three-dimensional schematic view of the absorber which we simulated is shown in Fig. 3.1. A periodic array of nano-spheres, which are embedded in a silica layer, are distributed according

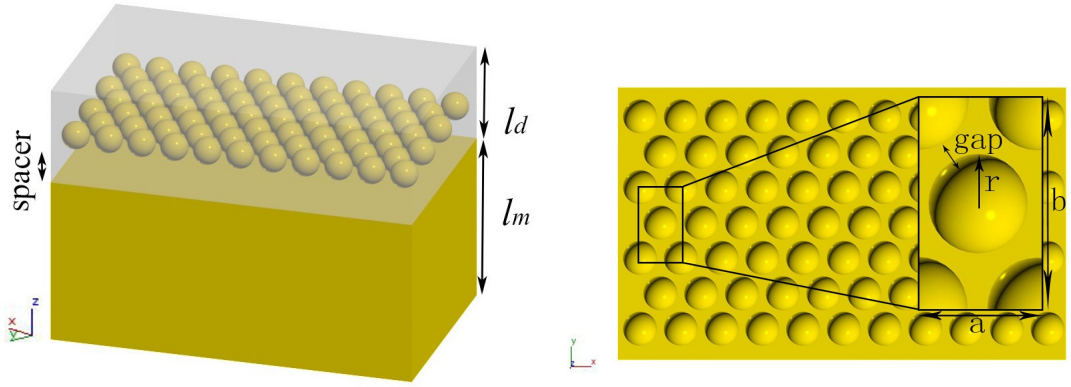

(a) (b)

Figure 3.1. (a) Three-dimensional schematic view of the gold nano-spheres based absorber; (b) Top view of the distribution of the gold nano-spheres.

to a triangular lattice on a continuous gold reflector. The nano-spheres and the gold reflector are separated by a *spacer*, which is a part of the silica film. In our simulations the parameters used are as followed unless otherwise specified.

- relative permittivity of silica: $\epsilon_{SiO_2} = 1.5^2$
- relative permittivity of gold : ϵ_{Au} is from the experimental data by P. B. Johnson and R. W. Christy [16]
- r=4 nm: the radius of the nano-sphere
- l_d=35 nm: the total thickness of the silica film
- *spacer*=10 nm: the distance from the bottom of the sphere to the bottom of the silica thinfilm
- l_m=100 nm: the thickness of the gold reflector
- *gap*=1 nm: the distance between the nearest neighboring spheres
- *alpha* = 0°: the incident angle
- *beta*=90°: *beta*=0° and *beta*=90° indicate the electric field along x and y direction respectively
- *lattice*: equilateral triangular lattice

- $reference\ surface$: the interface between the gold reflector and the silica layer, which is in x-y plane at $z = 0$

3.2 Simulation method

To investigate the distribution of the electromagnetic field inside and outside the structure at the resonant frequencies, we need to solve the Maxwell's equations. Due to the complexity of the structure, it is difficult to find an analytical solution. Thus, we use Finite Element Method (FEM), which is a numerical method to solve the partial differential equations, to solve the Maxwell's equations in frequency domain. The basic philosophy of FEM is to approximately treat continuous quantities as a set of quantities at discrete points, which are at nodes and edges. The more dense the mesh is, the more elements one has solving the problem; correspondingly one needs more memory and time. In our work, we use RF module for 3D structure of Comsol Multiphysics 4.2. Floquet periodic boundary condition and perfect match layer (PML) have been used in our study.

Moreover, we find the resonance frequency by calculating the absorbance of the structure from 400 nm to 800 nm. The absorbance is defined by $A = 1 - T - R$, in which T and R represent transmittance and reflectance respectively. T and R are calculated by performing surface integral of Poynting vector on the surface under the gold reflector and on the interface between the silica layer and the air. Since the 100 nm gold reflector is sufficiently thick to block the light from passing through the absorber, normally there is less than 1% leaking power.

3.3 Influence of geometry and dielectric environment

3.3.1 Sphere radius and gap

As radius is an important geometry dimension of an individual sphere, which affects all the four kinds of resonance we have mentioned above, we first simulate the structure with l_d=35 nm, *spacer*= 10 nm, *alpha*=0°, *beta*=90°, and *gap*=1 nm/3 nm to investigate the influence of r on the resonant wavelength.

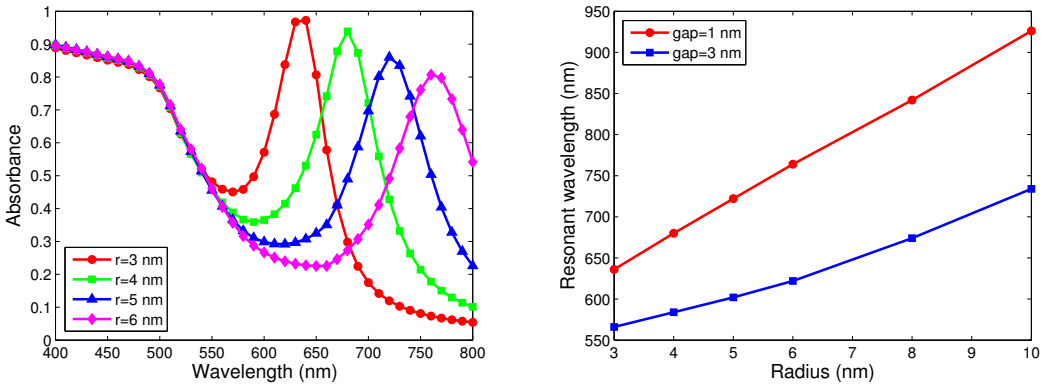

(a) (b)

Figure 3.2. Calculated (a) absorption spectra of the absorber as a function of sphere radius with gap=1 nm; (b) resonant wavelength as a function of sphere radius both with gap=1 nm and 3nm.

As shown in Fig. 3.2 (a), an increase in sphere radius shifts the resonant wavelength to the red. Additionally, Fig. 3.2(b) shows that the shifts in the resonant wavelength increase approximately linearly with increasing radius in this short range and it shifts faster for smaller gap structure.

For the sphere with a diameter less than 10 nm, we can neglect the phase

retardation effect and apply quasi-static approximation. Thus, if the resonance is due to dipole surface plasmon resonance of individual sphere, the resonant wavelength should satisfy the relation $Re[\epsilon_{Au}] + 2\epsilon_{SiO_2} = 0$ [18], which is located at around 530 nm and does not shift much with increasing sphere radius. However, the calculated resonant wavelength shows pronounced red-shift compared to that of individual sphere as predicted by quasi-static approximation. To find the reason, we further look into the field distribution at the resonance. The electric field distributions of the structure with r=4 nm, l_d=35 nm, gap=1 nm, $alpha$=0° both for E_x and E_y polarized light are shown in Fig. 3.3. Because the gold nano-spheres are placed in close proximity to each other, the near-field interparticle coupling becomes dominant [23]. For E_x polarized light, the resonance is mainly caused by the coupling between the neighbouring nano-spheres along x direction and for E_y polarized light, it is mainly due to the coupling between the middle sphere and the corner spheres. The electric field are well confined in the gap between neighbouring nano-spheres with thousands orders of magnitude higher than the incident field, which leads to the higher absorption of absorber. Moreover, we didn't see any couplings between the nano-spheres and the gold reflector, which is not the case for MIM structure absorber.

We further study the influence of the *gap* between neighbouring spheres. Fig. 3.4(a) shows the absorption spectra of the absorber for the structure with fixed r=4 nm as a function of *gap*. The increases in the *gap* contribute to the blue-shifts of resonant wavelength. Fig. 3.4 (b) also shows that, the shifts in resonant wavelength decay with increasing *gap*.

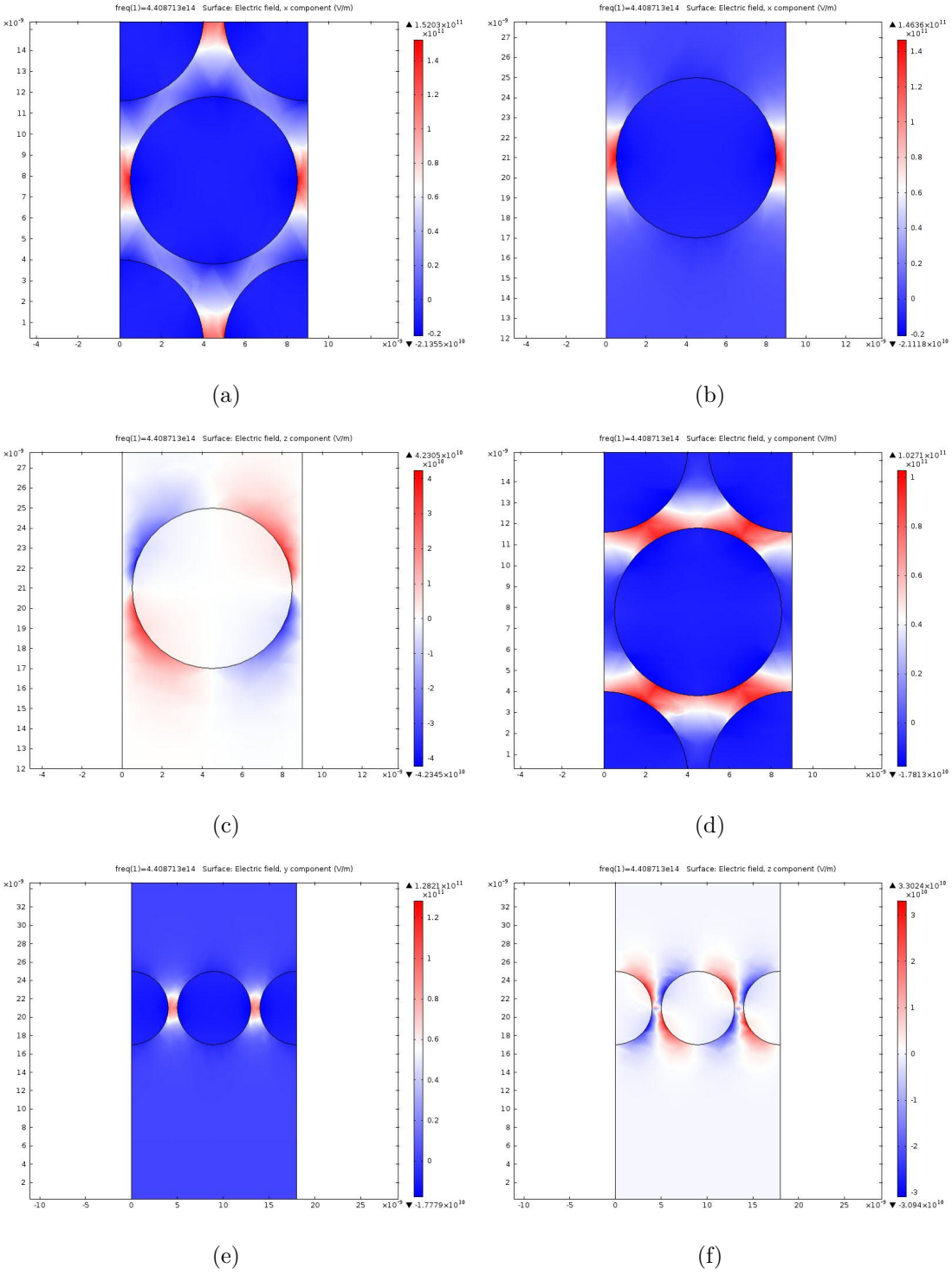

Figure 3.3. (a) Electric field x component in x-y plane at z=spacer+r; (b) Electric field x component in x-z plane at y=0; (c) Electric field z component in x-z plane at y=0 for E_x polarized incident field; (d) Electric field x component in x-y plane at z=spacer+r; (e) Electric field y component in diagonal plane; (f) Electric field y component in diagonal plane for E_y polarized incident field.

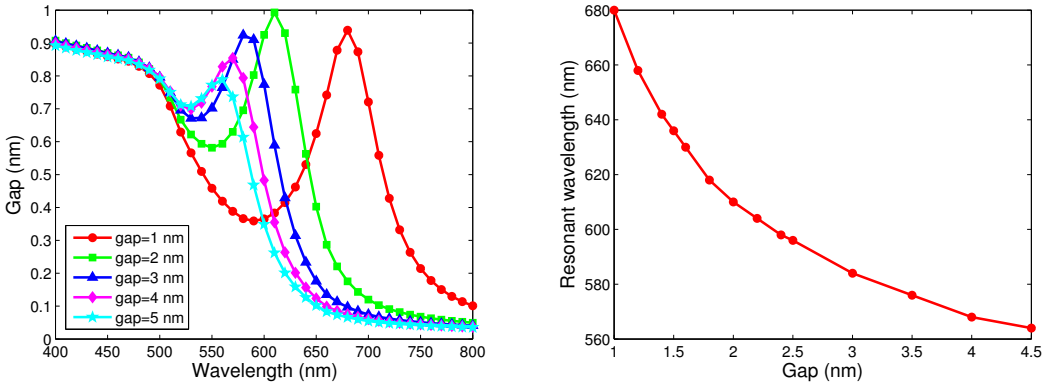

(a) (b)

Figure 3.4. (a)Calculated absorption spectra of the absorber as a function of gap with r=4 nm; (b) Calculated relationship between gap and resonant wavelength with r= 4nm.

To explain the influence of r and gap, we can apply dipolar coupling model [17]. Since the nano-spheres are subwavelength, the polarizability of an isolated gold particle with silica surrounding medium in quasi-approximation can be described by

$$\alpha = \epsilon_0 V(1+\kappa)\frac{\epsilon_{Au} - \epsilon_{SiO_2}}{\epsilon_{Au} + \kappa\epsilon_{SiO_2}} \tag{3.1}$$

in which V is the volume of the particle, ϵ_{Au} and ϵ_{SiO_2} are the relative permittivity of gold and silica respectively, and κ is a shape factor described the geometry of the particle. As we have discussed in Chapter 2, for a sphere $\kappa = 2$ [see Eq.(2.65)]. Here we simplify the problem as a two-sphere system. In the presence of a neighboring sphere, the electric field felt by each sphere

$$E' = E + \frac{p'}{2\pi\epsilon_{SiO_2}\epsilon_0 d^3} \tag{3.2}$$

consists of two part, one is the incident electric field E and another is the near field of the dipole electric field of the other sphere. Here d represents the distance from the sphere. Applying Eqs. (2.65), (3.1), (3.2) and $V = \frac{4}{3}\pi R^3$, we obtain [**?**]

$$\alpha' = \frac{16\pi\epsilon_0 R^3(\epsilon_{Au} - \epsilon_m)}{\epsilon_{Au}(4 - \frac{(2R)^3}{d^3}) + \epsilon_{SiO_2}(8 + \frac{(2R)^3}{d^3})} \tag{3.3}$$

Thus the LSPR condition can be expressed by

$$\epsilon_{Au} = -\epsilon_{SiO_2}\frac{8(s/2R+1)^3 + 1}{4(s/2R+1)^3 - 1} \tag{3.4}$$

in which s=d-D is the interparticle surface-to-surface separation. For the case of isolated particle which $s \to \infty$, Eq.(3.4) becomes Eq.(2.66). The effective κ can be written as

$$\kappa_{two-particle} = \frac{8(s/2R+1)^3 + 1}{4(s/2R+1)^3 - 1} \tag{3.5}$$

The relationship between radius and effective κ, and gap and effective κ are plotted in Fig. 3.5(a) and (b) respectively. The effective κ increases with increasing radius and decreasing in gap. As the real part of relative permittivity decrease when the wavelength shifts to the red, Eq. (3.4) can well explain the shifts in Fig. 3.2(a) and 3.3(a). Moreover, the change in effective κ is much faster for the same variation in gap than r. That's why we can see the shift with changing gap is more significant than that of changing r.

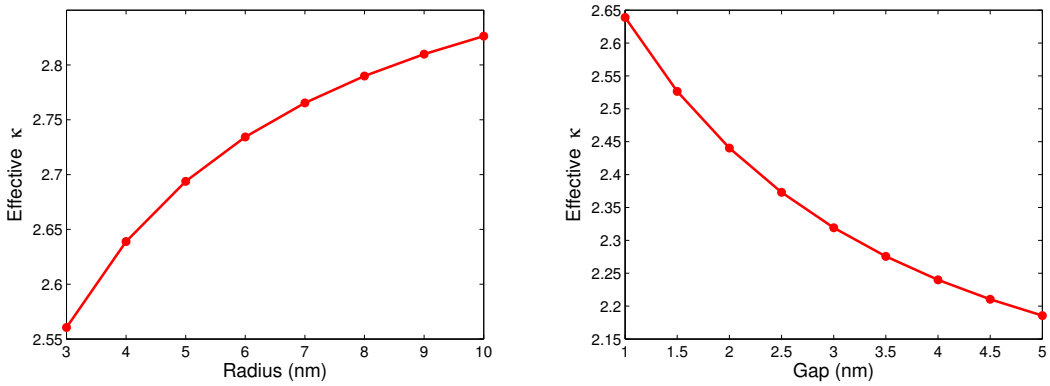

(a) (b)

Figure 3.5. Relationship between (a) r and effective κ with gap=1 nm; (b) gap and effective κ with r=4 nm.

3.3.2 Dielectric environment

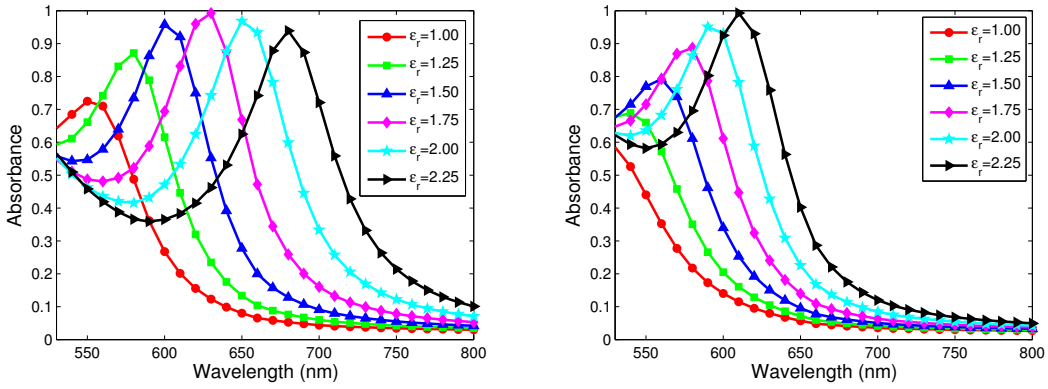

(a) (b)

Figure 3.6. Calculated absorption spectra of the absorber for the structure with r=4 nm (a) gap=1 nm; (b) gap=2 nm.

From Eq. (3.4) we know that besides the *radius* and *gap* the resonant wavelength also depends on the dielectric function ϵ_r of the surrounding medium. Fig. 3.6(a)

and (b) show the effect of the changing in ϵ_r for the structure with r=4 nm, gap=1 nm/2 nm.

As increase in dielectric function of the surrounding medium shifts the resonant peak to the red, which matches the prediction by Eq.(3.4). Moreover, the shifts for the structure with a smaller *gap* is more obvious that that for the structure with a larger *gap*. This advantage shows great potential of the structure with smaller gap size for sensing the variation in refractive (e.g. changing in concentration of the solution).

3.3.3 Spacer

Since we do not see any coupling between the nano-spheres and the gold reflector, we further change the thickness of *spacer* to see if there is any coupling. First, we fix r=4 nm, gap=1.8 nm, and the total thickness of the silica layer (include the layer with spheres) to be $spacer + 25\ nm$.

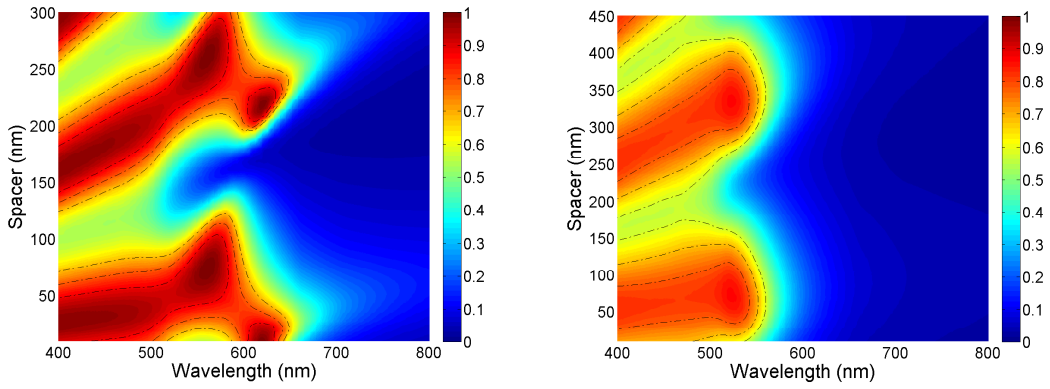

(a) (b)

Figure 3.7. Calculated absorption spectra of the absorber as a function of spacer with l_d=spacer+25nm, r=4 nm, gap=1.8 nm for the structure with gold reflector (a) in silica; (b) in air.

The absorption spectra are shown in Fig. 3.7(a) and (b) for the structure with silica and air surrounding medium respectively. As shown in the figure, both of the absorption spectra change periodically with increasing *spacer*. In Fig. 3.7(a), the resonant peak is at around 620 nm with maximum absorbance 99.7% with the $spacer \approx 210\ nm$. With this spacer, the total phase shifts of the incident field in the spacer is $\triangle\phi = \frac{2\pi}{\lambda} \cdot 2n \cdot spacer \approx 2\pi$, which leads to the constructive interference. Moreover, at some spacer thickness the absorption peak shifts to the blue. However, this is due to the overlap of the tail of the absorption spectra of the intrinsic absorption of gold and the absorption due to near-field interparticle coupling. It's because that when the *spacer* changes from 0 nm to around 180nm, the constructive interference at longer wavelength of overlap tail become dominate and when it increases to about 210 nm the constructive interference at shorter wavelength dominate again. We also carried out a simulation for the case of air surrounding medium, we don't see this small shift because of the peak due to near-field interparticle coupling and the intrinsic absorption are pretty near. Additionally, the peak due to interparticle coupling is not too much larger than the overlap part. As a result the shift is not obvious, but the changing is also periodic.

We further simulate the same structure in silica but without gold reflector. The absorption spectra of this structure are shown in Fig. 3.8. The spectra also change periodically with increasing *spacer* thickness and the period is nearly the same as that for the structure with gold reflector. The maximum value of the peak due to near-field interparticle coupling is about half of that for the structure with gold reflector. However ,the absorption is less than half of that for the structure with gold reflector. This is because the gold reflector also contributes to the absorption in the intrinsic absorption region. Thus basically the spacer act as a Fabry-Pérot Étalon. Besides, comparing to the structure with gold reflector, the peak due to

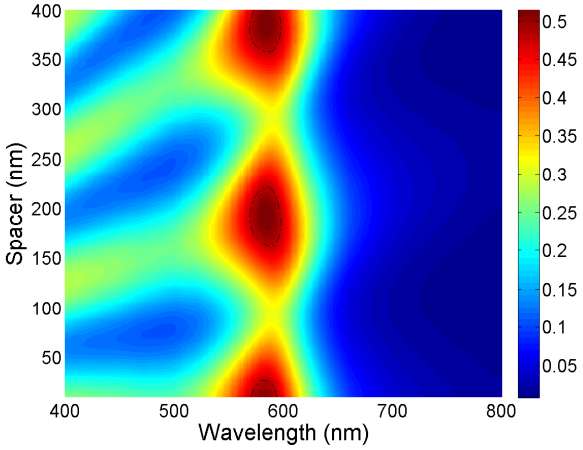

Figure 3.8. Calculated absorption spectra of the absorber as a function of spacer with l_d=spacer+25nm, r=4 nm, gap=1.8 nm for the structure without gold reflector in air

interparticle coupling slightly shifts to the blue.

3.4 Influence of incident angle and polarization

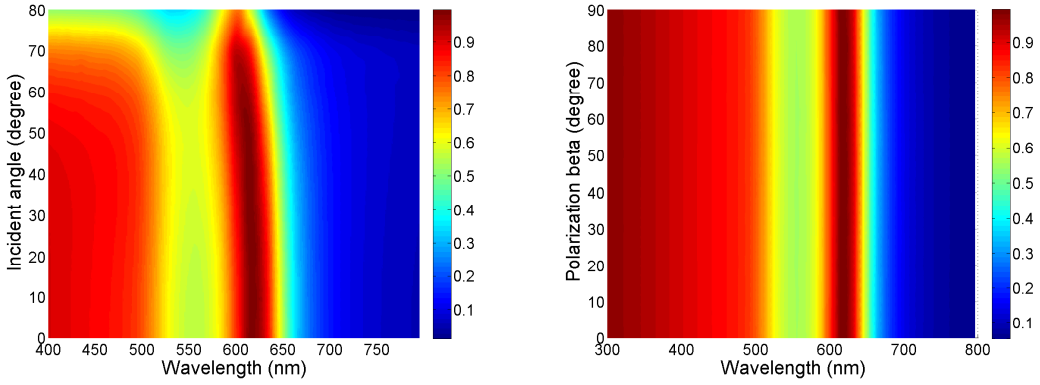

(a) (b)

Figure 3.9. Calculated absorption spectra of the absorber with r=4 nm and gap=1.8 nm as a function of (a) incident angle; (b) polarization angle.

Generally for many applications, it is desirable for an absorber to have absorption independent of incident or polarization angle. We simulate the absorber for the structure with r=4 nm and gap=1.8 nm. The absorption spectra of the absorber as a function of incident angle and polarization are shown in Fig. 3.9 (a) and (b) respectively. For the incident angle from 0° to 70°, and polarization from 0° to 90°, we get nearly the same optical response. We attribute this to the symmetric configuration of the nano-spheres.

3.5 Influence of lattice

All absorbers which we have discussed above have an equilateral triangular lattice. Here we stretch equilateral triangular lattice along x direction. After stretching, the *gap* between the middle and the four corner spheres is still 1.8 nm. However, the *gap* between the neighbouring spheres along x-axis direction becomes 1.8 nm. Thus the equilateral triangular lattice is changed to an isosceles triangular lattice. Here with simulated the structure with with this isosceles triangular lattice, r=4 nm. Fig. 3.10(a) shows the calculated absorption spectra of the absorber for both the structure with equilateral triangular and isosceles triangular lattice. The isosceles triangular breaks the symmetry of the configuration, thus it is not polarization-independent. Although the *gaps* between the middle and the four corner spheres are the same for these two lattice structures, the response for both E_x and E_y polarized incident are not the same. It is because we cannot simply think that the absorption is only due to the coupling between the neighbouring spheres along the electric field. The coupling along other direction also contribute to the absorption (see Fig. 3.11).

We further change the lattice of the structure to a square lattice with a lattice constant d and r=4 nm. As show in Fig. 3.10 (b), as increasing lattice constant,

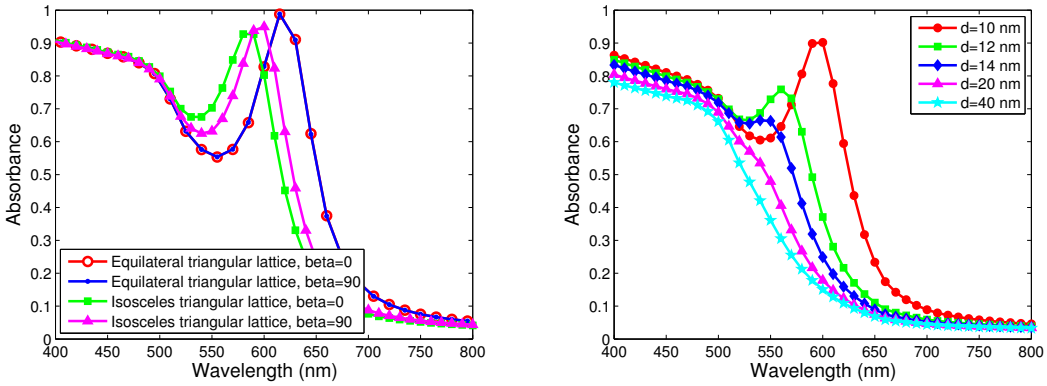

(a) (b)

Figure 3.10. Calculated absorption spectra of the absorber (a) for both of structure with equilateral triangular lattice and isosceles triangular lattice in E_x and E_y polarized incidence; (b) for the structure with a square lattice as a function of lattice constant d.

which means the *gap* between the neighboring spheres are getting larger, the resonant wavelength shifts to the blue. In addition, when the lattice constant becomes larger and larger, the resonance is getting closer to the pure dipole resonance of an individual sphere.

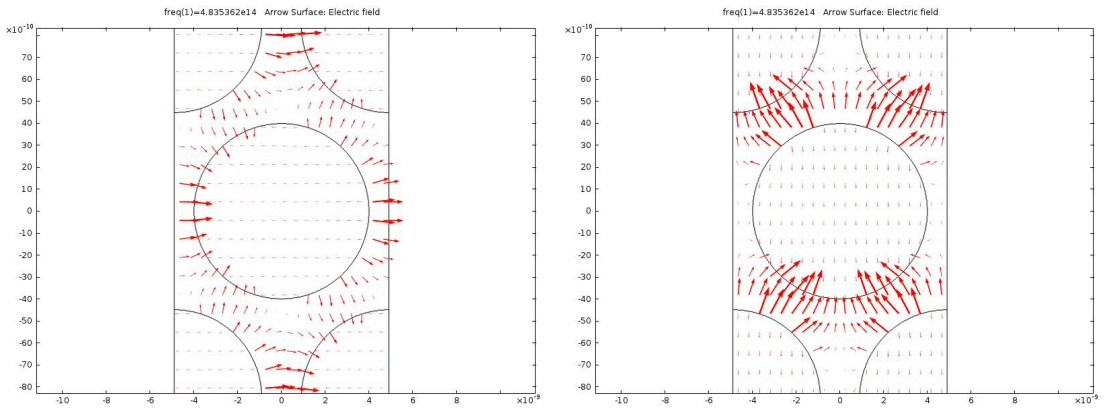

(a) (b)

Figure 3.11. Electric field arrow plot for the structure with r=4 nm, gap=1.8 nm, and equilateral triangular lattice in (a) E_x polarized field; (b) E_y polarized field.

3.6 Spheres of different sizes

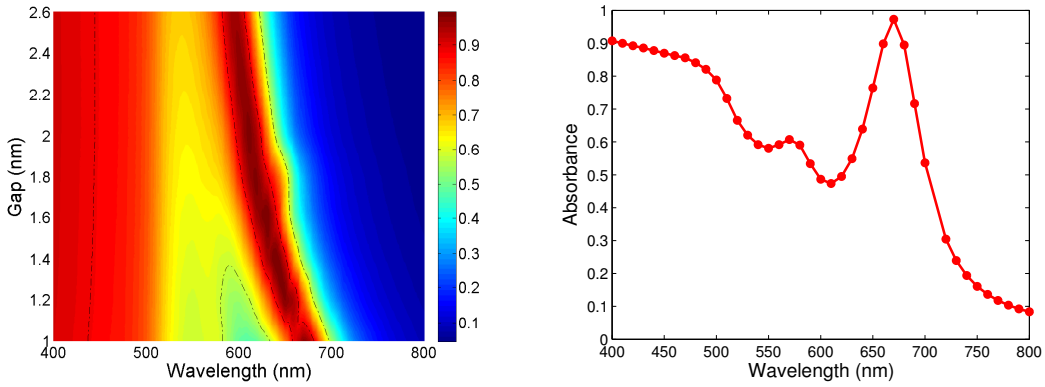

(a) (b)

Figure 3.12. Calculated absorption spectra of the absorber for the structure with different sphere sizes (a) as a function of gap; (b) at gap=1 nm.

In last session, we break the symmetric of the absorber by changing the lattice structure. Here, we break it by introducing nonuniformity in sphere sizes because it is too difficult to fabricate all the spheres of a same size. Instead of changing lattice structure, we change the size of four corner spheres, as shown in the inset of Fig. 3.1 (b), to 5 nm and keep the middle sphere radius at 4 nm. Our objective is to see whether the nonuniformity in sphere size will lead to a broadband absorption. Fig. 3.12 shows the absorption spectra of the absorber with this structure has two peaks at smaller *gap*. For the structure with *gap*=1 nm in E_x polarized incidence case, the *gap* between the middle spheres become 3 nm, thus it may have two absorption peaks due to different *gap* and r. However, as the *gap* increases, both of the blue-shifts of resonant wavelength due to decrease in r decay(see Fig. 3.2 and 3.4). As a result, for larger gap the absorption band can not be separated by a small change in sphere radius. The nonuniformity in both *radius* and *gap* have

the potential to broaden the absorption peak.

3.7 Influence of particle shape

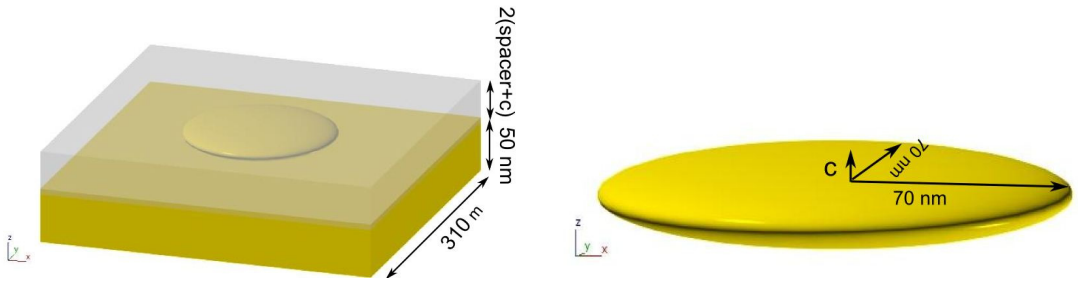

(a) (b)

Figure 3.13. (a) Three-dimensional schematic view of the gold nano-oblate spheroid based absorber; (b) Dimension of the oblate spheroid.

For traditional MIM absorbers, e.g. a rectangular shape nanoparticle based MIM absorber demonstrated by J. Hao et al. [24] with nearly total absorption, the bottom surface of nanoparticle is always parallel with the gold reflector surface. However, for a spherical nanoparticle it has a curved surface and this may be the reason why we didn't see any interaction between the nanoparticle and the gold reflector. To further investigate it, we simulate a structure with gold oblate spheroid embedded in silica on a gold substrate. As shown in Fig. 3.13, semi-major axis is 70 nm, the semi-minor axis is c, the lattice constant is 310 nm, the distance between the bottom point of the oblate spheroid is *spacer* which is fixed at 10 nm, the thickness of gold substrate is 50 nm, and the total thickness of the silica layer is equal to $2(spacer + c)$. In addition, the incident electric field is along the major axis with normal incidence. We gradually change the ratio r of minor

axis to major axis from 1:7 to 1, which means the shape of the particle changing from more oblate to more spherical.

The absorption spectra of the absorber for this structure is shown in Fig. 3.14. And the electric field distribution for the structure with c=20 nm at resonant frequencies are plotted in Fig. 3.15. We can clearly see the dipole resonance electric field pattern at 940 nm [see Fig. 3.15(a) (b) (c)], and the higher order resonance field pattern [21] at 580 nm [see Fig. 3.15(d) (e) (f)]. Two important conclusions can be drawn. First, the dipole resonance strongly depends on the geometry shape of the particle. With increasing the ratio r, the dipolar plasmon resonant wavelength shifts to the blue, which means comparing a sphere to an oblate spheroid with the same dimension along the electric field, the dipole plasmon resonant wavelength for a sphere is on the blue side of that of an oblate spheroid. Second, the higher order resonance at around 580 nm doesn't shift much with increasing r. In addition, as the ratio r increased, the dipole resonance become negligible when compared to higher order term.

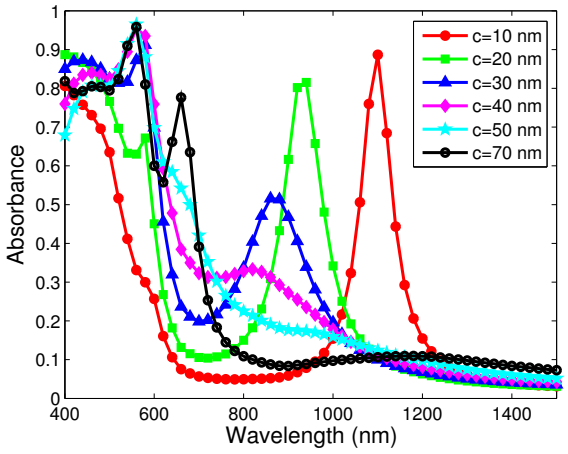

Figure 3.14. Calculated absorption spectra of the gold nano-oblate absorber as a function of c

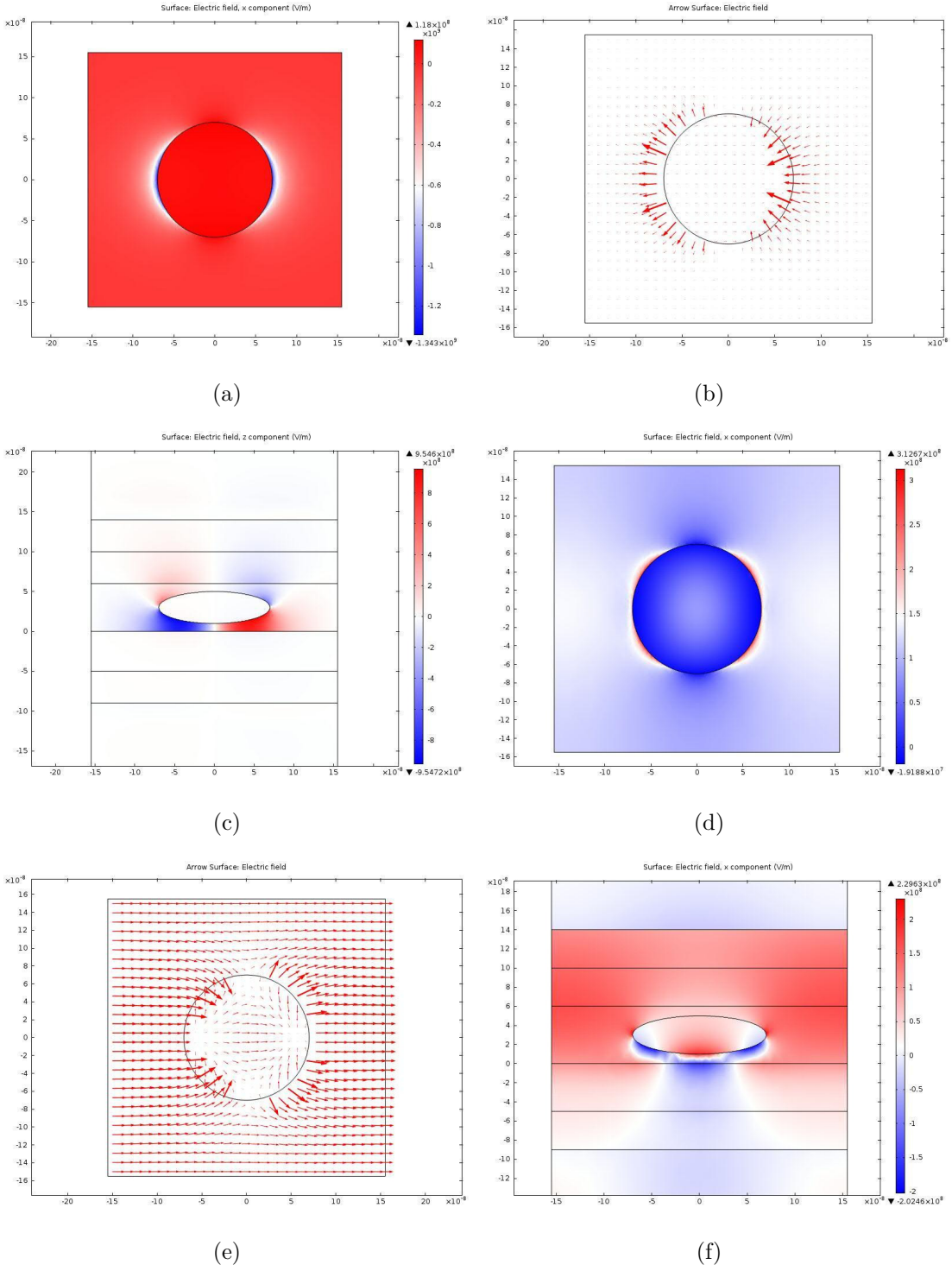

Figure 3.15. (a) Electric field x component in x-y plane at z=spacer+c for $\lambda = 940\ nm$; (b) Electric field arrow plot in x-y plane at z=spacer+c for $\lambda = 940\ nm$; (c) Electric field z component in x-z plane at y=0 for $\lambda = 940\ nm$; (d) Electric field x component in x-y plane at z=spacer+c for $\lambda = 580\ nm$; (e) Electric field arrow plot in x-y plane at z=spacer+c for $\lambda = 580\ nm$; (f) Electric field z component in x-y plane at at y=0 for $\lambda = 580\ nm$.

To give a general idea for the reason of the shifts due to variation in ratio r, we simply considering ellipsoid in the electrostatic approximation. The polarizabilities can be expressed by [21, 17]

$$\alpha_i = \frac{4\pi}{3} abc \frac{\epsilon - \epsilon_m}{\epsilon_m + L_i(\epsilon - \epsilon_m)} \tag{3.6}$$

L_i is the geometrical depolarization factor that depends on the shape of the particle with $i = a, b, c$ [25]. Moreover $\sum_i L_i = 1$, thus among L_a, L_b and L_c, only two are independent. For the oblate we have a=b and $L_a = L_b$. The depolarization factor

$$L_a = L_b = \frac{g(e)}{2e^2}[\frac{\pi}{2} - tan^{-1}g(e)] - \frac{g^2(e)}{2} \tag{3.7}$$

and

$$g(e) = (\frac{1 - e^2}{e^2})^{1/2} \tag{3.8}$$

in which e is the eccentricity which is equal to $\sqrt{1 - \frac{c^2}{a^2}}$. When a=c, which is the case for a sphere, we get $L_a = L_b = L_c = \frac{1}{3}$. For the case of a oblate we have $L_a = L_b < \frac{1}{3}$. The zeros of the denominator in Eq.(3.6) determine the resonant wavelength, thus

$$Re[\epsilon] = Re[(1 - \frac{1}{L_a})]\epsilon_m \tag{3.9}$$

Because the real part of relative permittivity of gold increases with blue shifts in wavelength, that's why the resonant peak of s sphere is on the blue-side of that of an oblate. In order to see the effects of substrate, we simulated the same structure but without gold reflector. The arrow plots in Fig. 3.16 clearly shows that the resonance at around 630 nm shown in Fig. 3.17 is due to dipole resonance. However, comparing the absorption spectra of the structure with gold reflector to

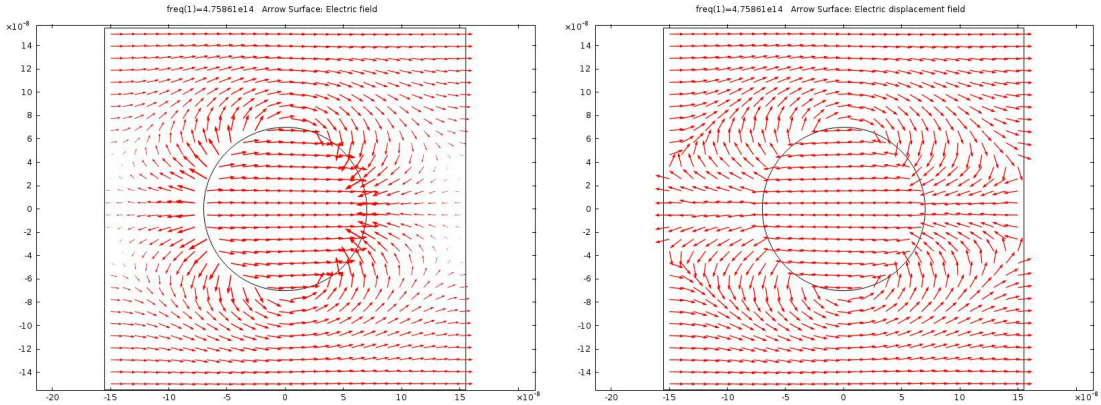

(a) (b)

Figure 3.16. Arrow plot of (a) electric field; (b) electric displacement field arrow plot for the gold nano-oblate absorber in x-y plane at z=spacer+c.

the structure without gold reflector, we can see significant red-shifts in dipole resonance peak. This is due to that the gold reflector breaks the symmetry of the medium. This can be described by introducing a mirror-image dipole which causes Van der Waals-like interactions with the particle [17]. It contributes to the red-shifts [26]

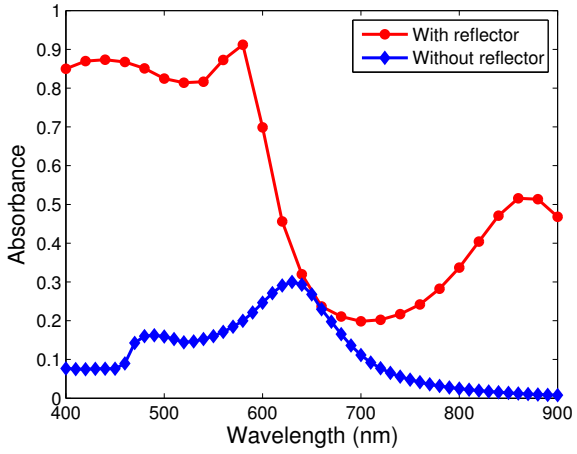

Figure 3.17. Calculated absorption spectra of the nano-oblate absorber with c=30 nm both for the structure with and without reflector

3.8 Multi-layer structure

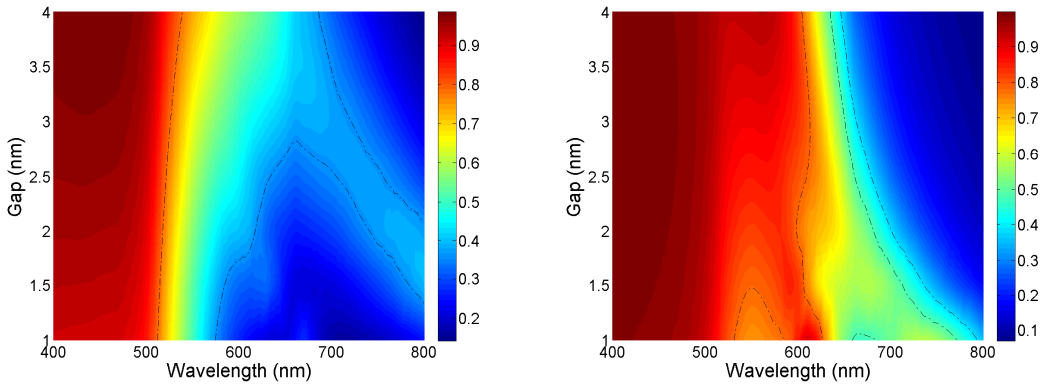

(a) (b)

Figure 3.18. Calculated absorption spectra of the nano-spheres based absorber for the structure with three layers of spheres with (a) the same radius r=5 nm; (b) with different size of spheres, from the top to the bottom layer, r=4.5 nm, r=4nm, r=3.5 nm respectively.

We also increase the layer of sphere to see if it can also improve the absorption of the absorber. We extend the structure in z direction and the nano-spheres are distributed in FCC like lattice. Fig. 3.18(a) and (b) show the absorption spectra for the structure with 3 layers of spheres. The former one is for 3 layers of sphere with r=5 nm. The latter is for the structure with 3 layers of spheres with r=4.5 nm, r=4 nm, r=3.5 nm respectively. From Fig. 3.18(b) we can see that the absorption band is nearly cover the whole visible range with a lowest absorption larger than 50% for $gap \approx 1$ nm. The multi-layers structure also provides us a possible way to broaden the absorption band.

3.9 Effective medium approximation

In 1904, J.C. Maxwell Garnett explains the color of gold ruby glass [27]. Since our silica layer is similar as the gold ruby glass, we follow Maxwell Garnett approxi-

mation to treat the silica film, which contains gold nano-spheres, as an effective medium. Since the gold particles are distributed homogeneously in the film, the optical response of the film can be assumed to be the average of the two components. For the absorber with multi-layers of our lattice structure, the volume fraction of gold can be written as

$$\phi = \frac{4/3\pi r^3 \times 4}{(2r + gap) \cdot \sqrt{3}(2r + gap) \cdot \sqrt{3}(2r + gap)} \approx \frac{0.585 r^3}{(2r + gap)^3} \tag{3.10}$$

then we obtain the average electric field

$$E_{av} = (1 - \phi)E_m + \phi E_I \tag{3.11}$$

and the average polarization

$$P_{av} = (1 - \phi)(\epsilon_{SiO_2} - 1)\epsilon_0 E_m + \phi(\epsilon_{Au} - 1)\epsilon_0 E_I = (\epsilon_{av} - 1)\epsilon_0 E_{av} \tag{3.12}$$

in which ϵ_{SiO_2} and ϵ_{Au} are the relative permittivities of silica and gold respectively, and E_I and E_m are the electric fields inside the sphere and within the matrix respectively. Moreover, the relationship between the field inside and outside the sphere can be described by

$$E_I = \frac{3\epsilon_{SiO_2}}{\epsilon_{Au} + 2\epsilon_{SiO_2}} E_m \tag{3.13}$$

Hence, the average electric field becomes

$$E_{av} = (1 - \phi)E_m + \frac{3\phi\epsilon_{SiO_2}}{\epsilon_{Au} + 2\epsilon_{SiO_2}} E_m \tag{3.14}$$

Combination of (3.2)(3.2)(3.4)(3.5) yields

$$\epsilon_{av} = \epsilon_{SiO_2} \frac{\epsilon_{Au}(1+2\phi) + 2\epsilon_{SiO_2}(1-\phi)}{\epsilon_{Au}(1-\phi) + \epsilon_{SiO_2}(2+\phi)} \tag{3.15}$$

The real part and imaginary part of the relative permittivity of the effective thin film based on Maxwell Garnett approximation are shown in Fig. 3.19(a) and (b) respectively. We use the dielectric function calculated from Maxwell Garnett

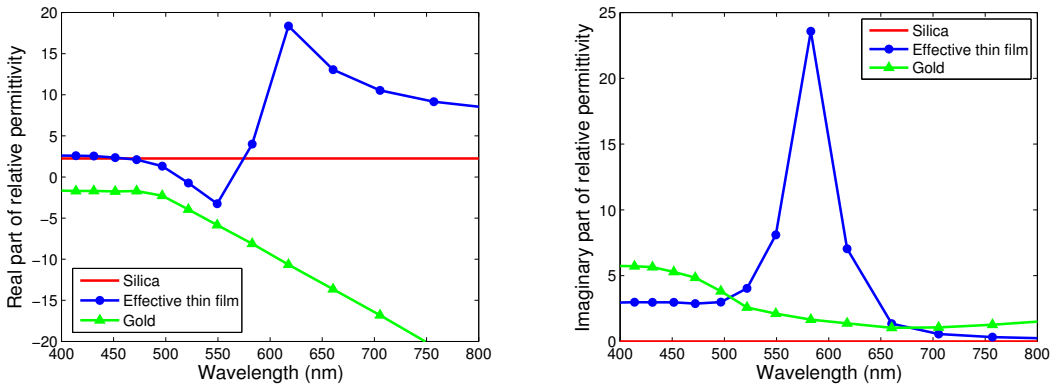

(a) (b)

Figure 3.19. (a) Real part of relative permittivity of the effective thin film vs silica; (b) Imaginary part of relative permittivity of the effective thin film vs gold.

approximation and treat the silica layer containing gold nano-spheres as an effective thin film to simulate nano-spheres absorber for the structure with 6 layer of spheres, r=5 nm, gap=2.5 nm, film thickness=65 nm and spacer =10nm both for the structure with and without gold reflector. The calculated absorption spectra for the structure without gold reflector and with gold reflector are shown in Fig. 3.20(a) and (b) respectively. Generally, the absorption spectra calculated using Maxwell Garnett approximation fit the calculated results of the nano-spheres structure well. However, in the region from 550 nm to 600 nm, there is a small peak. We attribute this to the resonance in dielectric function of the effective layer,

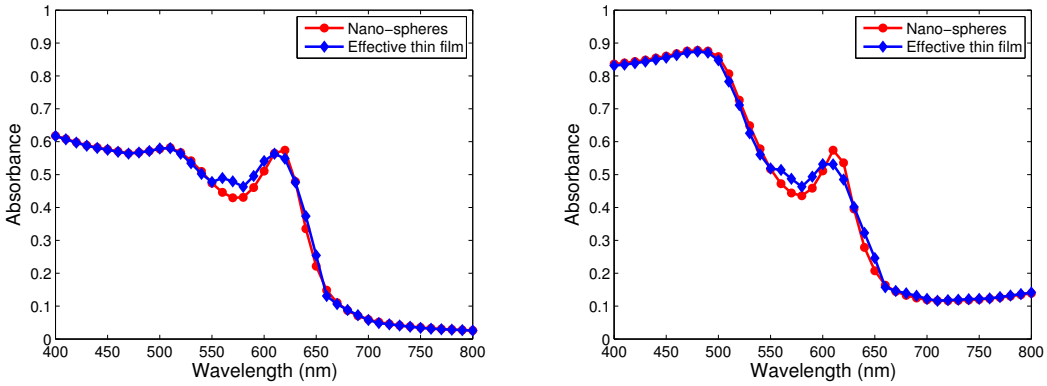

(a) (b)

Figure 3.20. Calculated absorption spectra of the nano-spheres absorber for the structure (a) without gold reflector; (b) with gold reflector.

which is resulted from Maxwell Garnett approximation, as shown in Fig 3.19.

3.10 Influence of MFP effect

At last, we study the influence of MFP effect on the optical response of our structure. We use the relative permittivity from Fig. 2.4(a) to simulate the single layer structure with r=4 nm. Fig. 3.21(a) and (b) the absorption spectra as a function of *gap*.

The MFP effect mainly contributes to the broadening of the absorption band, but in the meantime it will lower the maximum absorption value by about 10%. This is due to that the MFP effect increases the imaginary part of the relative permittivity for smaller particles [see Fig. 2.4(b)].

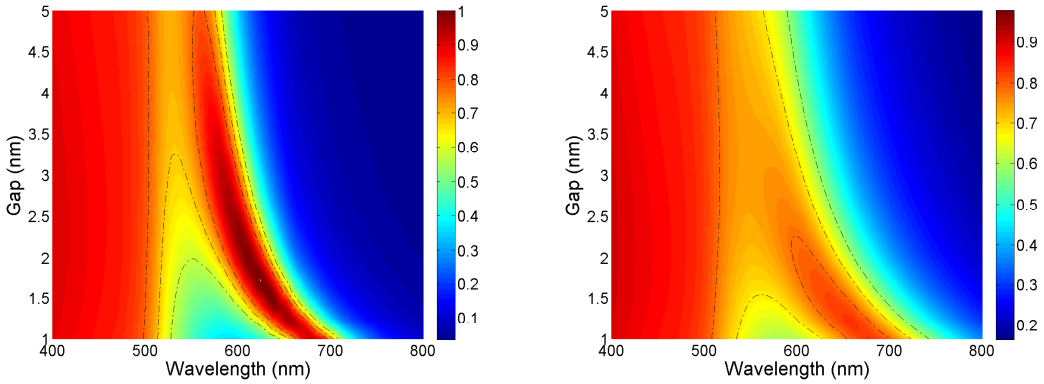

(a) (b)

Figure 3.21. Calculated absorption spectra of the nano-spheres absorber for the structure with r=4nm (a) without considering MFP effect; (b) considering MFP effect.

Chapter 4

Fabrication and Characterization

4.1 Au@SiO2 core-shell nanoparticles based absorber

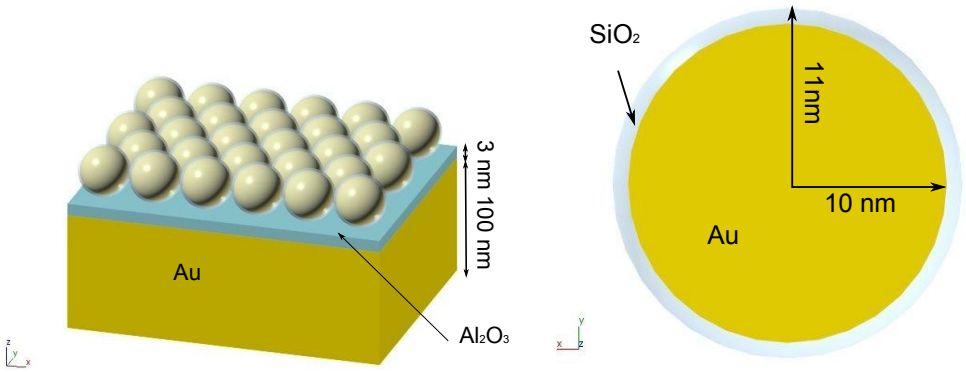

(a) (b)

Figure 4.1. (a) Three-dimensional schematic view of Au@SiO_2 core-shell nanoparticles based absorber ; (b) The cross section view of the Au@siO_2 nanoparticles.

Based on the simulations we have presented in Chapter 3, we proposed a novel design of a plasmonic absorber based on Au@SiO_2 core-shell nanoparticles. Fig.

4.1(a) shows the three-dimensional schematic view of the absorber. The radius of the Au particle is 10 nm and the silica shell thickness is 1 nm. The resonant wavelength was designed at around 780 nm (see Fig. 4.5(a)).

4.2 Fabrication process

4.2.1 Substrate preparation

4 nm titanium, 100 nm gold and followed 3 nm aluminium oxide were deposited on silicon dioxide substrate using Provac PAK 600 Coating System which uses Electron beam physical vapor deposition(EBPVD) method to perform the deposition. The chamber base pressure is 5E-7 mbar and process pressure is 5E-6 mbar. The deposition speed for titanium, gold , and aluminium oxide are 0.5 Å/s, 1 Å/s and 0.5 Å/s respectively.

4.2.2 Au@SiO_2 core-shell nanoparticles preparation

Gold nanoparticles were prepared chemically via a sol-gel method [28], by reducing 10 mM hydrochloroauric acid ($HAuCl_4$) using 20 mM ascorbic acid and 1 mM sodium borohydride ($NaBH_4$) in the presence of aqueous solution of cetyltrimethyl ammonium bromide (CTAB, 0.2 M) and silver nitrate ($AgNO_3$, 2 mM) at room temperature. The mixture was stirred for one hour and kept at 25° overnight. To coat the gold nanoparticles with silica shell, 1 mL of obtained suspension of gold nanoparticles was diluted to 20 mL and the pH was tuned to ca. 12. When the temperature of this suspension was elevated to 70° , 5 μL of tetraethyl orthosilicate (TEOS) was added, and the solution was collected after 1 h reaction and centrifuged to obtained silica-coated gold nanoparticles (Au@SiO_2). The morphology of Au and Au@SiO2 nanoparticles, as shown in Fig. 4.2, was char-

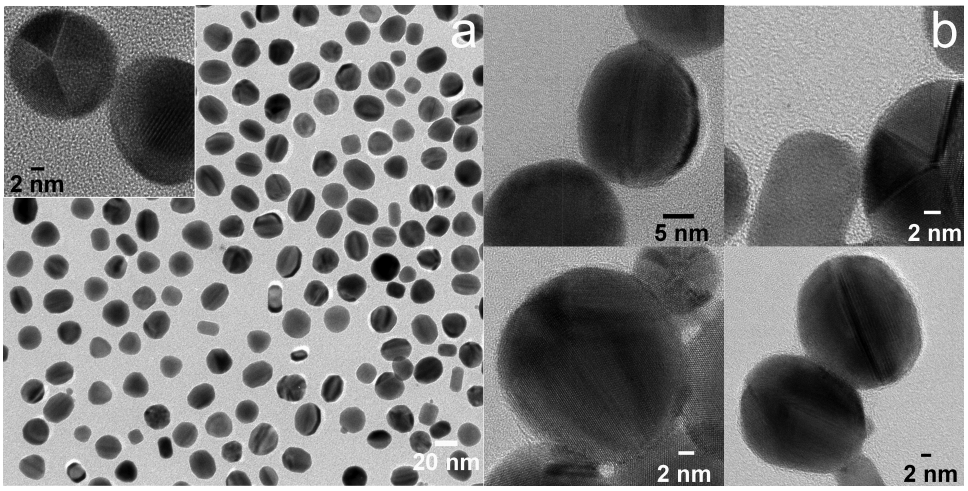

Figure 4.2. TEM micrographs of (a) Au nanoparticles;(b) Au@SiO_2 core-shell nanoparticles

acterized by JEM-2100F field emission transmission electron microscope (TEM) operating at accelerating voltage of 200 kV. The concentration of gold in colloidal suspensions was measured by Inductively coupled plasma atomic emission spectroscopy (ICP-AES). The concentration of gold (element) and number of nanoparticles in Au@SiO2 suspension are about, Au: $120ppm(\mu g/mL)$; nanoparticle: $1.505 \times 10^{22}/mL$. In addition, the Au@SiO_2 nanoparticles in aqueous solution have a dark red color(see Fig. 4.3).

4.2.3 Particle deposition

We first tried to deposit the Au@SiO_2 nanoparticles by spinning. The particles were deposited onto the substrate by using a 100 μl pipette drop by drop during spinning. However, due to the hydrophobicity of Aluminium oxide we failed to achieve that. At lower rotation speed around 800 rpm the the drop cannot be spread out. However, at higher speed the drop is quickly span away. We didn't find a speed in between which can well spread the particles on the substrate. Finally, we use a 10 μl pipette to deposit the particles on the substrate without

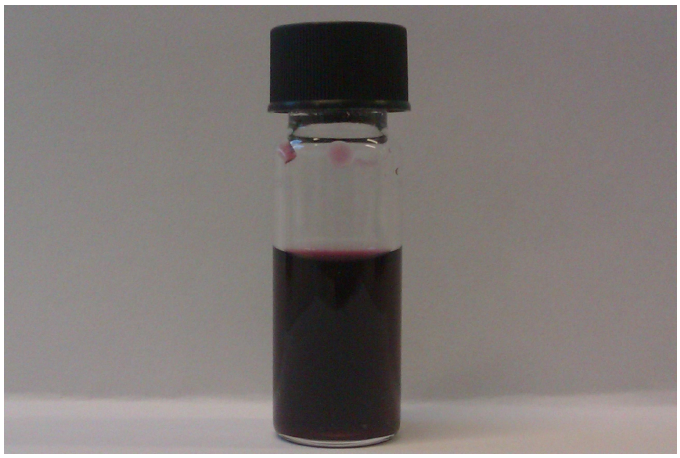

Figure 4.3. Appearance of the Au@SiO_2 suspensions

spinning. Totally 170μl Au@SiO_2 colloidal suspensions have been put on the substrate. After that, we bake it in the oven for 2 hours at 70° at low pressure.

4.3 Optical properties

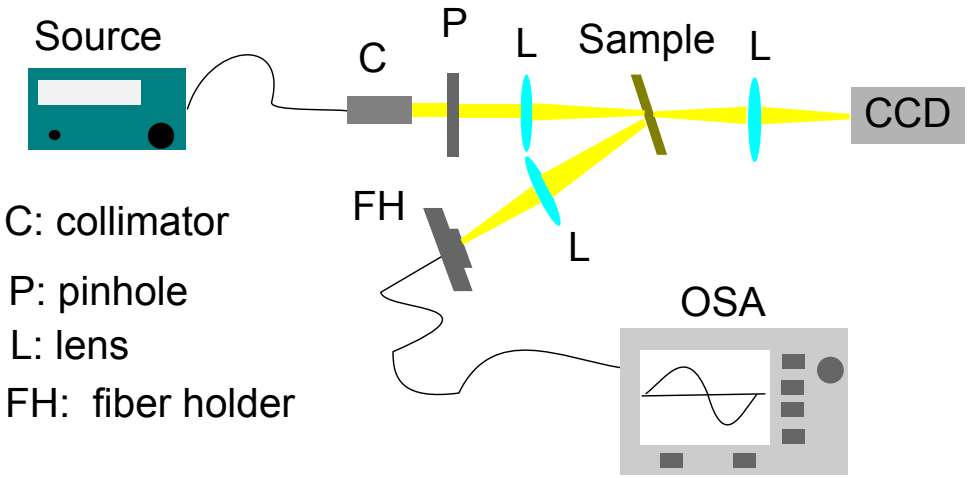

Figure 4.4. Schematic setup for the reflectance measurement

The setup for measuring reflectance is demonstrated in Fig. 4.4. A white light source (NKT superK Compact) with a repetition rate of 27 KHz is connect with

a reflective collimator through a multi-mode fiber. The collimated beam diameter is about 8.5 mm. The collimated beam is then pass through a 600μm pinhole. And then the beam is focused by an aspherized achromatic lens (f=45 mm) on to the sample. On the back side of the sample, a 20× objective (f=200mm) and a CCD camera monitored with a PC are used to track the position of the beam. The reflected light was focused by another aspherized achromatic lens on the fiber core to couple the reflected light into a multi-mode fiber which connected to the OSA.

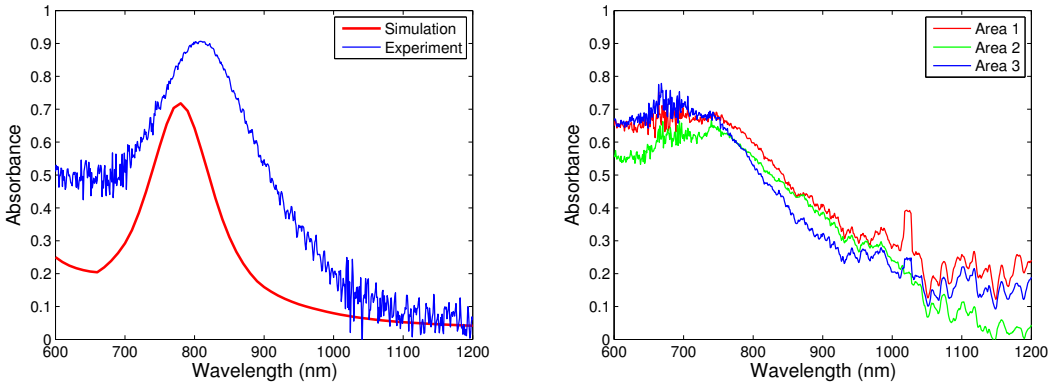

(a) (b)

Figure 4.5. Measured absorption spectra of the fabricated absorber (a) with focusing lens ; (b) Without focusing lens.

Fig. 4.5(a) and (b) show the measured absorption spectrum of the fabricated sample at 15° incident angle using the system with focusing lens (0.1 mm beam diameter) and without focusing lens (2 mm beam diameter) respectively. As shown in Fig. 4.5(a), the shape of simulated and measured absorption spectra are similar. Due to the inhomogeneous distribution of Au@SiO_2 nanoparticles, the high absorption only occurred at several certain positions. We make a mark around these positions and capture it with the CCD camera [see Fig. 4.6(a)]. SEM image with respect to the captured beam position is shown in Fig. 4.5(b). The coverage of

these areas is around 80% which is better than most of the other parts. However, the measured the absorption band is broader than that of the simulated one. We attribute this to the inhomogeneous in gold sphere radius, silica shell thickness and also the arrangement of $Au@SiO_2$ core-shell particles [see Fig. 4.7(a)]. Because of surface roughness, not all of the scattered light was coupling into the fiber. As a result, the absorbtion is higher than we get from simulations. For the absorption

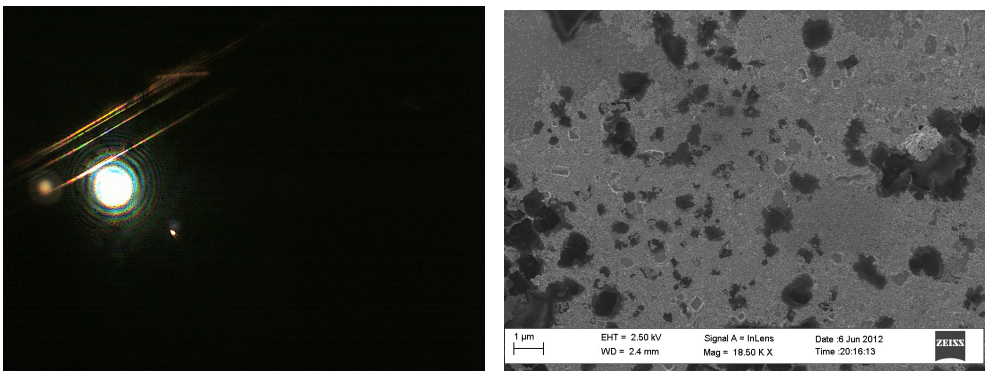

(a) (b)

Figure 4.6. (a) CCD captured view of the beam position ; (b) SEM image of $Au@SiO_2$ particles according to the beam position area.

spectra measured without lens (2 mm beam diameter), the average absorption value is lower but more broader than the well covered small area measured with lens. It's because the variation in particle size and arrangement are of a wider range than that of a small area [see Fig. 4.7].

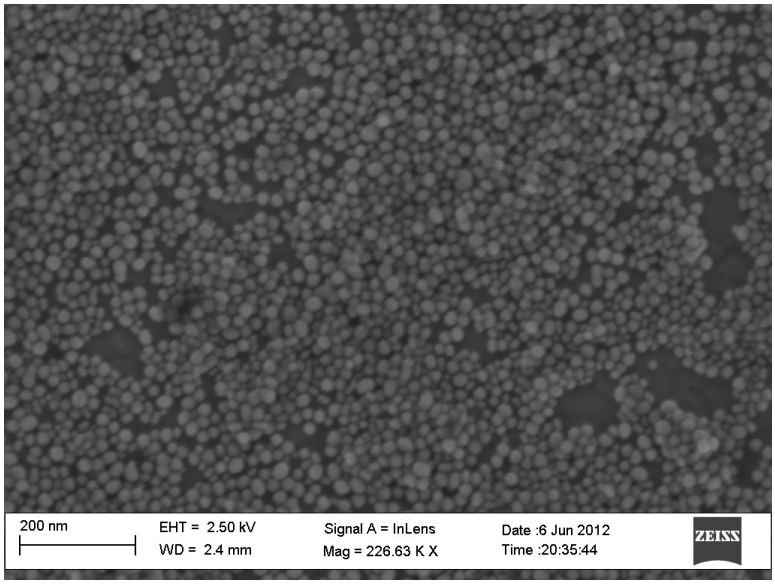

(a)

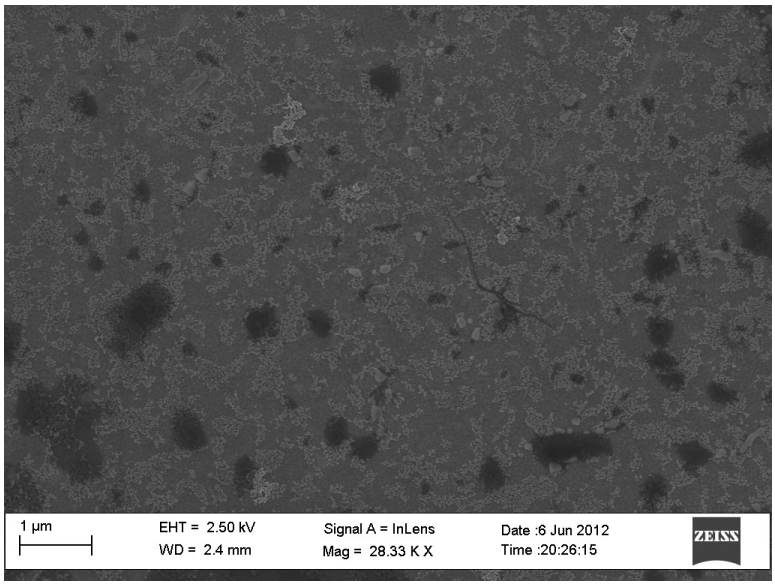

(b)

Figure 4.7. SEM image of (a) Au@SiO_2 particles at good coverage area ; (b) Au@SiO_2 particles at bad coverage area.

Chapter 5

Conclusion and Outlook

5.1 Conclusion

Due to the strong near field interparticle coupling, nano-spheres based plasmonic absorber strongly confines the electromagnetic field between neighbouring particles, which leads to a polarization-independent and wide angle absorption. The absorption spectra range can be tuned from visible to near-infrared by simply change the size of the particle or the separation between each particle. Difference in sphere size, gap and multi-layer structure supply us a great opportunity to achieve broad-band absorption. Moreover, for the structure with smaller interparticle separation, the resonant wavelength is much more sensitive to the change of dielectric function of the surrounding medium. This property can be further utilized in sensing the change in refractive index. The function of the spacer and gold reflector is not the same as traditional MIM absorbers. The gold particle layer, spacer, and the gold reflector form a Fabry-Pérot Étalon. We also treat the gold nanoparticles layer as a effective thin film layer using Maxwell Garnett approximation and as the number of layer increases, the predicted resonant wavelength are well matched with the simulation results.

We fabricated a Au@Si_2 core-shell nanoparticle based absorber which has more than 50% absorption from 600nm to 900 nm, the peak is centered at around 800 nm. However, due to the inhomogeneous in particle coverage, this good performance can only be observed in several of these certain areas.

5.2 Outlook

The inhomogeneous distribution of the nanoparticles need to be solved in order to make a better performance absorber. We can also decrease the particles to tune it into visible regime. Moreover, the properties of this kind of absorber needs to be exploited in sensing use. We also need to built up a new setup for measuring the absorbance more precisely and also in the visible regime in the future.

Bibliography

[1] W. Cai and V. Shalaev, *Optical Metamaterials* (Springer New York Dordrecht Heidelberg London).

[2] M. L. Brongersma and P. G. Kik, *Surface Plasmon Nanophotonics* (Springer, P.O. Box 17, 3300 AA Dordrecht, The Netherlands.).

[3] K. L. Kelly, E. Coronado, L. L. Zhao, and G. C. Schatz, "The optical properties of metal nanoparticles: The influence of size, shape, and dielectric environment," The Journal of Physical Chemistry B **107**, 668–677 (2003).

[4] E. M. Hicks, S. Zou, G. C. Schatz, K. G. Spears, R. P. Van Duyne, L. Gunnarsson, T. Rindzevicius, B. Kasemo, and M. Käll, "Controlling plasmon line shapes through diffractive coupling in linear arrays of cylindrical nanoparticles fabricated by electron beam lithography," Nano Letters **5**, 1065–1070 (2005).

[5] M. Burresi, D. Diessel, D. v. Oosten, S. Linden, M. Wegener, and L. Kuipers, "Negative-index metamaterials: Looking into the unit cell," Nano Letters **10**, 2480–2483 (2010).

[6] C. J. Brinker, Y. Lu, A. Sellinger, and H. Fan, "Evaporation-induced self-assembly: Nanostructures made easy," Advanced Materials **11**, 579–585 (1999).

[7] N. Liu, M. Mesch, T. Weiss, M. Hentschel, and H. Giessen, "Infrared perfect absorber and its application as plasmonic sensor," Nano Letters **10**, 2342–2348 (2010).

[8] A. Atwater, Harry A.and Polman, "Plasmonics for improved photovoltaic devices," Nat Mater **9**, 205–213 (2010).

[9] M. K. Hedayati, M. Javaherirahim, B. Mozooni, R. Abdelaziz, A. Tavassolizadeh, V. S. K. Chakravadhanula, V. Zaporojtchenko, T. Strunkus, F. Faupel, and M. Elbahri, "Design of a perfect black absorber at visible

frequencies using plasmonic metamaterials," Advanced Materials **23**, 5410–5414 (2011).

[10] K. Neyts, J. Danckaert, P. Tassin, P. V. Brabant, J. Beeckman, and I. Veretennicoff, "Optical materials syllabus," University of Ghent and Vrije Universiteit Brussel.

[11] P. Drude, "Zur elektronentheorie der metalle," Annalen der Physik **306**, 566–613 (1900).

[12] P. Drude, "Zur elektronentheorie der metalle; ii. teil. galvanomagnetische und thermomagnetische effecte," Annalen der Physik **308**, 369–402 (1900).

[13] C. Kittel, *Introduction To Solid State Physics* (Wiley, 2005).

[14] W. Harrison, *Solid state theory*, International series in pure and applied physics (McGraw-Hill, 1970).

[15] A. D. Rakic, A. B. Djurišic, J. M. Elazar, and M. L. Majewski, "Optical properties of metallic films for vertical-cavity optoelectronic devices," Appl. Opt. **37**, 5271–5283 (1998).

[16] P. B. Johnson and R. W. Christy, "Optical constants of the noble metals," Phys. Rev. B **6**, 4370–4379 (1972).

[17] U. Kreibig and M. Vollmer, *Optical Properties of Metal Clusters*, Springer Series in Materials Science (Springer, 2010).

[18] S. Maier, *Plasmonics: Fundamentals And Applications* (Springer, 2007).

[19] G. Mie, "Beiträge zur optik trüber medien, speziell kolloidaler metallösungen," Annalen der Physik **330**, 377–445 (1908).

[20] P. Debye, "Der lichtdruck auf kugeln von beliebigem material," Annalen der Physik **30**.

[21] C. Bohren and D. Huffman, *Absorption and Scattering of Light by Small Particles*, Wiley Science Series (John Wiley & Sons, 2008).

[22] F. Yu, H. Wang, and S. Zou, "Efficient and tunable light trapping thin films," The Journal of Physical Chemistry C **114**, 2066–2069 (2010).

[23] H. Xu, E. J. Bjerneld, M. Käll, and L. Börjesson, "Spectroscopy of single hemoglobin molecules by surface enhanced raman scattering," Phys. Rev. Lett. **83**, 4357–4360 (1999).

[24] J. Hao, L. Zhou, and M. Qiu, "Nearly total absorption of light and heat generation by plasmonic metamaterials," Phys. Rev. B **83**, 165107 (2011).

[25] E. C. Stoner, "The demagnetizing factors for ellipsoids," Annalen der Physik **36**.

[26] T. Yamaguchi, S. Yoshida, and A. Kinbara, "Optical effect of the substrate on the anomalous absorption of aggregated silver films," Thin Solid Films **21**, 173 – 187 (1974).

[27] J. C. M. Garnett, "Colours in metal glasses and in metallic films," Philosophical Transactions of the Royal Society of London. Series A, Containing Papers of a Mathematical or Physical Character **203**, 385–420 (1904).

[28] L. Dong, F. Ye, A. Chughtai, S. Popov, A. T. Friberg, and M. Muhammed, "Photostability of lasing process from water solution of rhodamine 6g with gold nanoparticles," Opt. Lett. **37**, 34–36 (2012).